ASTM INTERNATIONAL

Geotechnical Testing Journal

Amalesh Jana,[1] Aleyna M. Donaldson,[2] Armin W. Stuedlein,[3] and T. Matthew Evans[1]

DOI: 10.1520/GTJ20190426

Deep, In Situ Nonlinear Dynamic Testing of Soil with Controlled Blasting: Instrumentation, Calibration, and Application to a Plastic Silt Deposit

Geotechnical Testing Journal

doi:10.1520/GTJ20190426 available online at www.astm.org

Amalesh Jana,[1] Aleyna M. Donaldson,[2] Armin W. Stuedlein,[3] and T. Matthew Evans[1]

Deep, In Situ Nonlinear Dynamic Testing of Soil with Controlled Blasting: Instrumentation, Calibration, and Application to a Plastic Silt Deposit

Reference

A. Jana, A. M. Donaldson, A. W. Stuedlein, and T. M. Evans, "Deep, In Situ Nonlinear Dynamic Testing of Soil with Controlled Blasting: Instrumentation, Calibration, and Application to a Plastic Silt Deposit," *Geotechnical Testing Journal* https://doi.org/10.1520/GTJ20190426

ABSTRACT

This study presents a novel test method to obtain dynamic properties of soil in situ using controlled blasting. Experimental and calibration protocols have been developed to conduct such investigations for any soil at any depth to obtain the coupled response between nonlinear shear modulus and pore pressure generation in soil. Controlled blasting using buried explosives with different charge weights at various depths were used as an active seismic source and the soil response measured. Micro electro mechanical system (MEMS) accelerometers, geophones, pore pressure transducers, and the MEMS-based inclinometers were calibrated to develop unique excitation voltage-to-unit relationships. Procedures to determine the post-installation sensor locations and orientations were developed to quantify the appropriate body wave velocity and shear strain in the soil. The conversion of calculated strains to a constant-volume direct simple shear-equivalent shear strain facilitated direct comparison to previously reported shear modulus reduction curves. Although this manuscript primarily focuses on instrumentation and calibration protocols, an example of the results of a test blast program is provided to demonstrate observation of the in situ, coupled, nonlinear fluid-mechanical response of an instrumented plastic silt deposit at a depth of 9 to 11.5 m below ground surface.

Keywords

cyclic and dynamic properties of soils, geophysics, field testing

Manuscript received November 20, 2019; accepted for publication October 1, 2020; published online January 11, 2021.

[1] School of Civil and Construction Engineering, Oregon State University, 101 Kearney Hall, Corvallis, OR 97331, USA

[2] Cornforth Consultants, 10250 SW Greenburg Rd., Suite 111, Portland, OR 97223, USA

[3] School of Civil and Construction Engineering, Oregon State University, 101 Kearney Hall, Corvallis, OR 97331, USA (Corresponding author), e-mail: armin.stuedlein@oregonstate.edu, https://orcid.org/0000-0002-6265-9906

Introduction

Characterization of the nonlinear cyclic stress-strain response of soil deposits represents a critical exercise in seismic site response and numerical deformation analyses. Robust determination of constitutive model parameters that can be used to predict soil response under dynamic loading is critically important, yet significant engineering judgment is often required over the course of such investigations. Hence, researchers and practitioners alike continue to press for improved understanding of the coupled, fluid-mechanical inelastic response of soils under dynamic loading as novel testing techniques are developed and existing methods refined. Laboratory studies have provided key insights into the cyclic response of soils, including such critical parameters as the threshold shear strain corresponding to the departure of linear elastic shear response, γ_{te} (e.g., Stokoe et al. 1995; Darendeli 2001; Menq 2003), initiation of residual excess pore pressures generation, γ_{tp} (Dobry et al. 1982, 1985; Vucetic and Dobry 1986, 1988; Ohara and Matsuda 1988; Matasović and Vucetic 1992, 1995; Vucetic 1994; Hsu and Vucetic 2006; Derakhshandi et al. 2008; Mortezaie and Vucetic 2016), and liquefaction triggering curves (e.g., Idriss and Boulanger 2008). Moreover, laboratory studies on intact specimens, such as those on silt (e.g., Dahl et al. 2014; Wijewickreme, Soysa, and Verma 2019), provide a strong basis for calibration of dynamic constitutive models. Although numerous laboratory studies on reconstituted and natural soil specimens have been performed to aid the understanding of general trends in cyclic response, the former cannot capture the effects of aging, soil fabric, and deposition-induced anisotropy, and the latter are frequently affected by sample disturbance or disturbance during specimen preparation, or both. Additionally, the effect of drainage during shaking, which is of particular concern to those regions affected by long-duration subduction zone earthquakes, cannot easily be captured using laboratory element tests. Thus, the testing of natural soil deposits in their in situ state is both useful and directly applicable in practice.

Few studies have been conducted to characterize the in situ dynamic response of soils. Henke and Henke (2002) reported the use of a torsional cylindrical impulse shear test device to infer the nonlinear dynamic properties of soil without pore pressure measurement. Riemer and Cobos-Roa (2007) used a downhole freestanding shear device to characterize the in situ shear modulus degradation of plastic soft Bay Mud; however, excess pore pressures were not measured. Kurtulus and Stokoe (2008) dynamically loaded a drilled shaft to generate cylindrical, axisymmetric shearing in a partially saturated, low-plasticity silt deposit where shear modulus degradation was deduced using measurements of shear wave velocity, V_s. Excess pore pressures arising from the dynamic testing were not measured. The development of pore pressure in dynamically loaded soil is important because it contributes to the loss of strength, the magnitude of post-shaking volumetric strain, and the accumulation of permanent lateral deformations (Lee and Albaisa 1974; Dahl et al. 2014). The lack of coupled measurements of shear modulus reduction and excess pore pressure necessitates a comprehensive undertaking to understand the in situ dynamic soil response.

Recently, significant advances toward characterization of the in situ coupled, cyclic shear-induced excess pore pressure and nonlinearity of soil have been made using a mobile shaker truck (Rathje, Chang, and Stokoe 2005; Cox, Stokoe, and Rathje 2009; Roberts et al. 2016). The technique relies upon the use of custom instrumentation and surface loading that generates vertically propagating horizontally polarized shear waves, providing a direct analog of earthquake-induced ground motions. One of the primary limitations of mobile shaking is that it is restricted to shallow depths (typically 3 to 4 m; van Ballegooy et al., n.d.). Further, the soil layer overlying the target depths should be sufficiently stiff to transmit the surface energy throughout the test program (i.e., it should not soften during the test and dampen the applied loading).

Although controlled blasting techniques have been successfully used to quantify the consequences of liquefaction at great depths in unimproved and improved soils (e.g., Gohl et al. 1998, 2000; Gohl, Howie, and Rea 2001; Gohl, Martin, and Elliot 2009; Ashford et al. 2006; Charlie, Jacobs, and Doehring 1992; Charlie et al. 2013; Rollins, Gerber, et al. 2005; Rollins, Lane, et al. 2005; Wentz et al. 2015; Gianella and Stuedlein 2017; Amoroso et al. 2017, 2020; Fontana et al. 2019), the application of blasting to quantify the inelastic, coupled soil response over many orders of shear stain has not been comprehensively investigated. Much of the previous research on the

fundamental response of soil to blasting has focused on the near-field, *P*-wave dominated region (e.g., Charlie, Jacobs, and Doehring 1992; Charlie et al. 2013), whereas the use of controlled blasting to study the combined near-field and far-field dynamic response of soil has been limited.

Previous efforts to develop instruments, analytical techniques, and resulting coupled soil responses provide the basis to leverage controlled blasting as a source of near- and far-field seismic waves with which to dynamically shear soil at any depth and in any deposit (e.g., gravels, clean sands, silts and clays) and to observe degradation of shear stiffness and generation of excess pore pressures. This article focuses on the experimental procedures needed to conduct deep, blast-induced liquefaction/cyclic softening experiments to obtain appropriate dynamic soil characteristics at any depth. First, a test site and corresponding subsurface conditions are described, with emphasis on the plastic silt deposit for which an example application of controlled blasting to deduce its dynamic properties is provided herein. Then, the instruments and calibration protocols necessary to observe the in situ dynamic and post-shaking performance of soils are presented. Critical field procedures necessary to determine instrument locations and orientations are described. The article concludes with the results of a test blast program to demonstrate observation of the in situ, nonlinear, coupled fluid-mechanical response of an instrumented plastic silt deposit, which is made possible using controlled blasting.

Site Layout and Subsurface Conditions

The test site is located approximately 1.2 km southeast from, and aligned with, the south runway at Portland International Airport, which is owned and operated by the Port of Portland. Portland International Airport is situated along the Columbia River approximately 9 m above mean sea level within the Portland basin, and subject to various seismic hazards (e.g., the Cascadia Subduction Zone, Portland Hills Fault). **Figure 1*A*** presents the 45-m-long, linear blast array and subsurface explorations arranged along an East-West alignment. The various components comprising the experimental program include blast casings, grouted inclinometer casings with sondex settlement rings, cased and uncased boreholes for field vane shear testing, pore pressure transducers (PPTs), and custom geophones. Instrumented sensor arrays were installed in two different soil deposits to capture their dynamic response: the sand array is centered at a depth of 25 m within a medium dense clean to silty sand deposit, whereas the silt array is centered at a depth of 10.22 m within a plastic silt deposit, described in detail below.

The subsurface was explored using cone penetration tests with pore pressure measurement (CPTu) and mud-rotary borings for split-spoon sampling, standard penetration tests, and thin-walled tube sampling. Downhole geophysical testing was conducted to provide baseline compression (*P*-) and shear (*S*-) wave velocities. Subsurface explorations adjacent to the linear blast array (and not shown in **fig. 1**) included seismic CPTu and mud-rotary borings with various sampling techniques. Hydraulic fill sand and silty sand extends from the ground surface to a depth of 5 to 6 m and is underlain by a 2-m-thick layer of native loose, clean sand (**fig. 1*B***). Thereafter, a 5- to 6-m-thick, medium stiff plastic silt deposit extends to a depth of 12 to 13 m and is described in detail later in the article, followed by a deep deposit of medium dense, poorly-graded fine clean sand and sand with silt, with fines content, *FC*, ranging from 3 to 12 %. The depths of the deep sand and shallow silt arrays were selected based on the consideration of the spatial variability revealed by the CPTu, although some variation in soil consistency and relative density was observed in samples retrieved from these locations.

Figure 2*A*–*D* present the subsurface profile of the plastic silt deposit evaluated using a test blast program as described herein. The corrected cone tip resistance, q_t, and soil behavior type index (SBT; Robertson and Wride 1998), I_c, with depth is presented in **figure 2*A*** for CPT-3, located closest to the mud-rotary borings B-4 and B-6 (within 1.8 and 3.0 m; **fig. 1*A***) used for sampling and sensor installation. **Figure 2*A*** indicates that I_c typically varies from 2.9 to 3.1 for this silt deposit. **Figure 2*B*** presents the variation of Atterberg limits and natural water content, w_c, with depth, indicating that the plastic index, *PI*, ranged from 17 to 39, with an average of 28 (corresponding to high-plasticity silt [MH]). **Figure 2*C*** compares the in situ shear wave velocity of the soil in its initial state obtained from downhole and crosshole geophysical tests (Donaldson 2019) with the laboratory-based V_s measurements of intact soil specimens. The average downhole and crosshole shear wave velocity of the silt was

FIG. 1 Overview of test site: (*A*) site and exploration plan showing blast casings and instrumentation arrays aligned along the due east and west alignment, and (*B*) subsurface profile indicating location of the silt array.

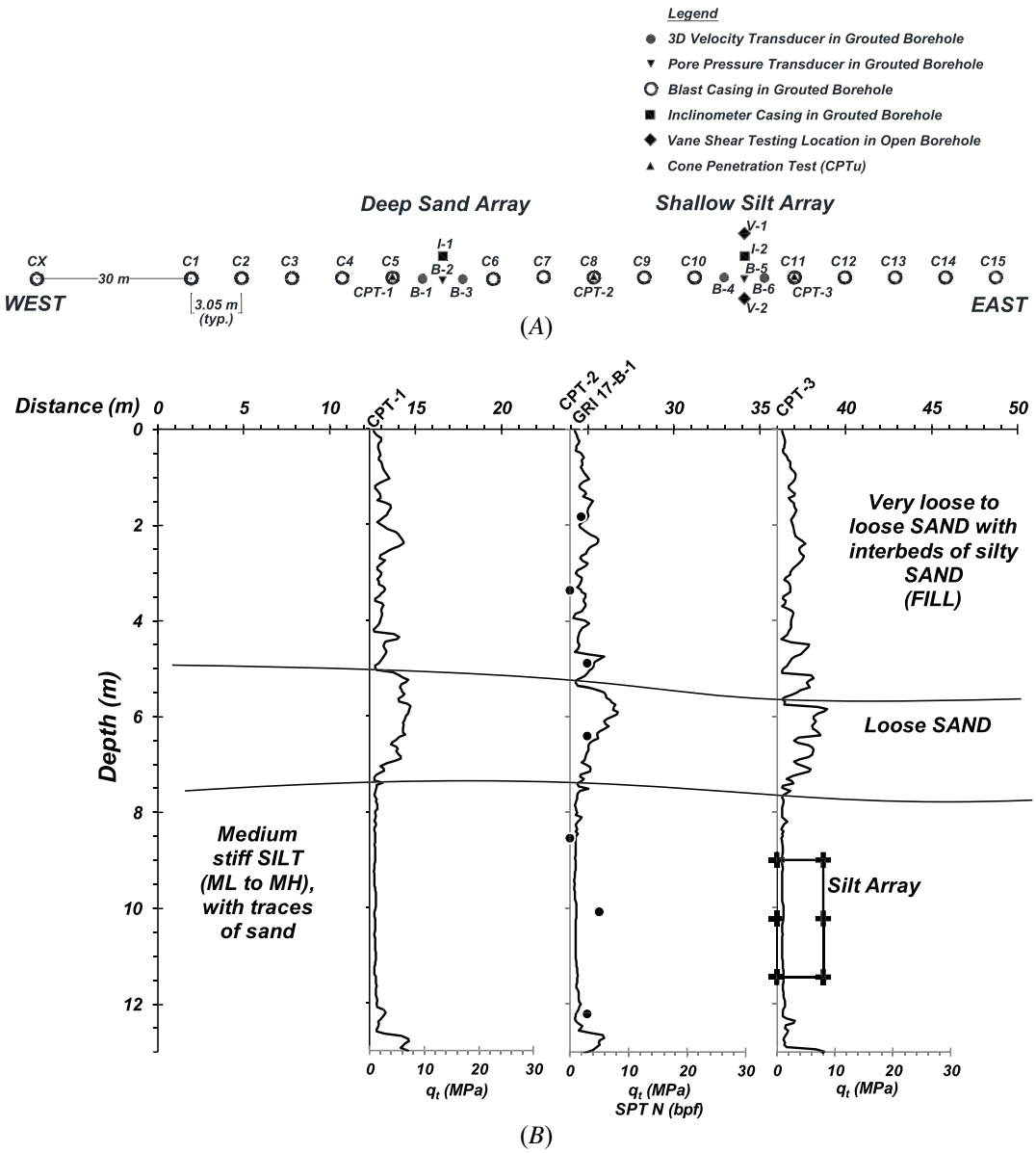

131 m/s and 123 m/s respectively. Similar estimates of V_s were obtained using the Andrus et al. (2007) CPT-based correlation (**fig. 2C**). **Figure 2D** presents the depth-varying overconsolidation ratio (*OCR*) derived from laboratory specimens to that determined using Mayne's (2007) correlation to q_t using CPT-3. The CPT-based *OCR*s increase slightly with depth and q_t, but they can be represented by a constant *OCR* of about 1.8 to 2.0.

Instrumentation and Calibration Protocols

Significant effort and care is necessary to capture the in situ dynamic response of natural soils, ranging from selection or development, or both, of appropriate instruments and provision of certain protective housings and

FIG. 2 Geotechnical characteristics of the plastic silt deposit including (*A*) cone tip resistance and SBT for CPT-3, (*B*) Atterberg limits and water content, (*C*) comparison of laboratory specimen- and in situ-based shear wave velocity, and (*D*) overconsolidation ratio. All laboratory specimens were retrieved from borings B-4 and B-6.

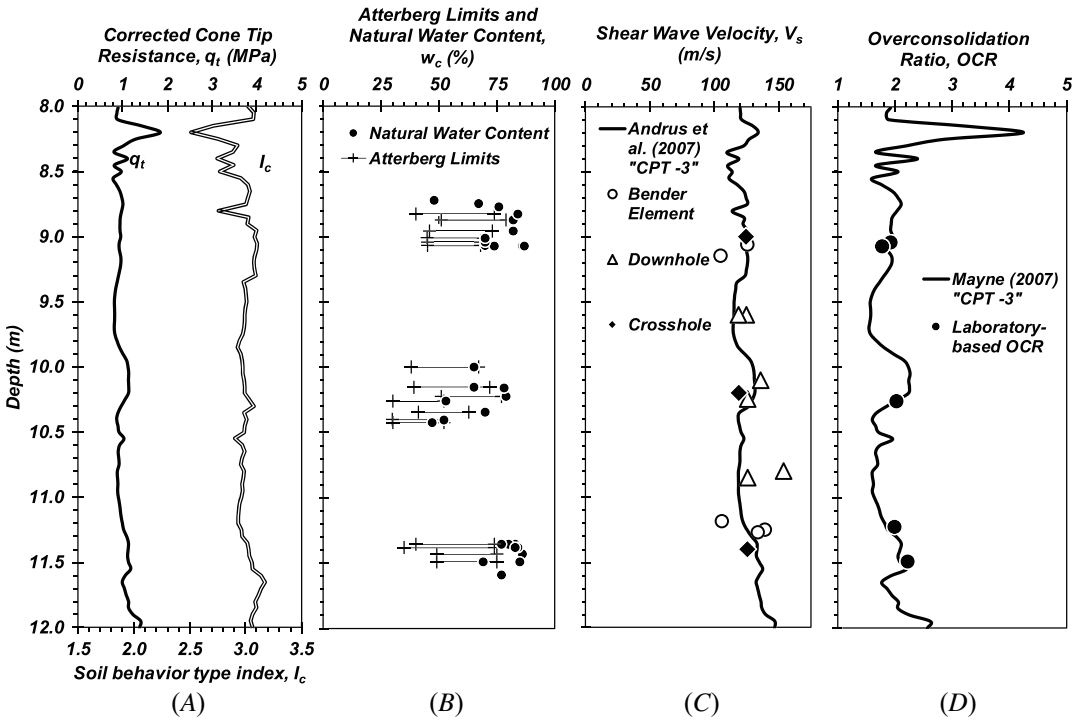

installation procedures. The distance between geophones must be carefully documented in order to accurately quantify body wave velocities, which forms the basis for characterization of the soil's dynamic mechanical properties. Mud-rotary boreholes were used to access the depths of interest and construct the instrumented soil arrays. Each array consisted of a minimum of four boreholes to (1) install a full-depth inclinometer casing fitted with sondex settlements rings, (2) install a string of PPTs, and (3) place two strings of custom-made triaxial geophone packages (TGPs). The geometry of the as-built arrays is shown in **figure 3**, designed after the novel protocols developed by Cox, Stokoe, and Rathje (2009) to back-calculate the change in shear modulus and excess pore pressure with shear strain following the finite element methodology first proposed by Rathje, Chang, and Stokoe (2005), Chang et al. (2007), Cox, Stokoe, and Rathje (2009) and subsequently implemented by Stokoe et al. (2014), Sahadewa et al. (2015), and Roberts et al. (2016, 2017), among others. Inclinometer casings were used to observe borehole deviation from vertical and to track the actual as-built horizontal position of the TGPs. Sondex settlement rings were attached to the inclinometers I-1 and I-2 (**fig. 1A**) to observe the local vertical deformation in close proximity to the TGPs and PPTs and facilitate computation of the corresponding volumetric strains following various blasting events.

PPTs AND THEIR CALIBRATION

PPTs were used to measure the initial hydrostatic and seismic *P*- and *S*-wave-induced excess pore pressures in the two arrays. Because of the substantial differences in hydrostatic and hydrodynamic pore pressures, PPTs must meet several requirements when used with controlled blasting, ranging from the ability to withstand pressures in the tens of MPa to providing an accuracy of less than 1 kPa if focused on near-surface soils (Rollins, Lane, et al. 2005). The amplified pressure transducer Model Unik 5000 A5034-TA-A3-CA-H0-PF manufactured by GE Measurement and Control (2014) was found to perform satisfactorily in controlled blasting experiments reported

FIG. 3 Elevation view of the as-built (*A*) silt array and (*B*) sand array. For clarity, boreholes housing inclinometer casing with sondex rings and surface sensors are not shown here (all units are in m).

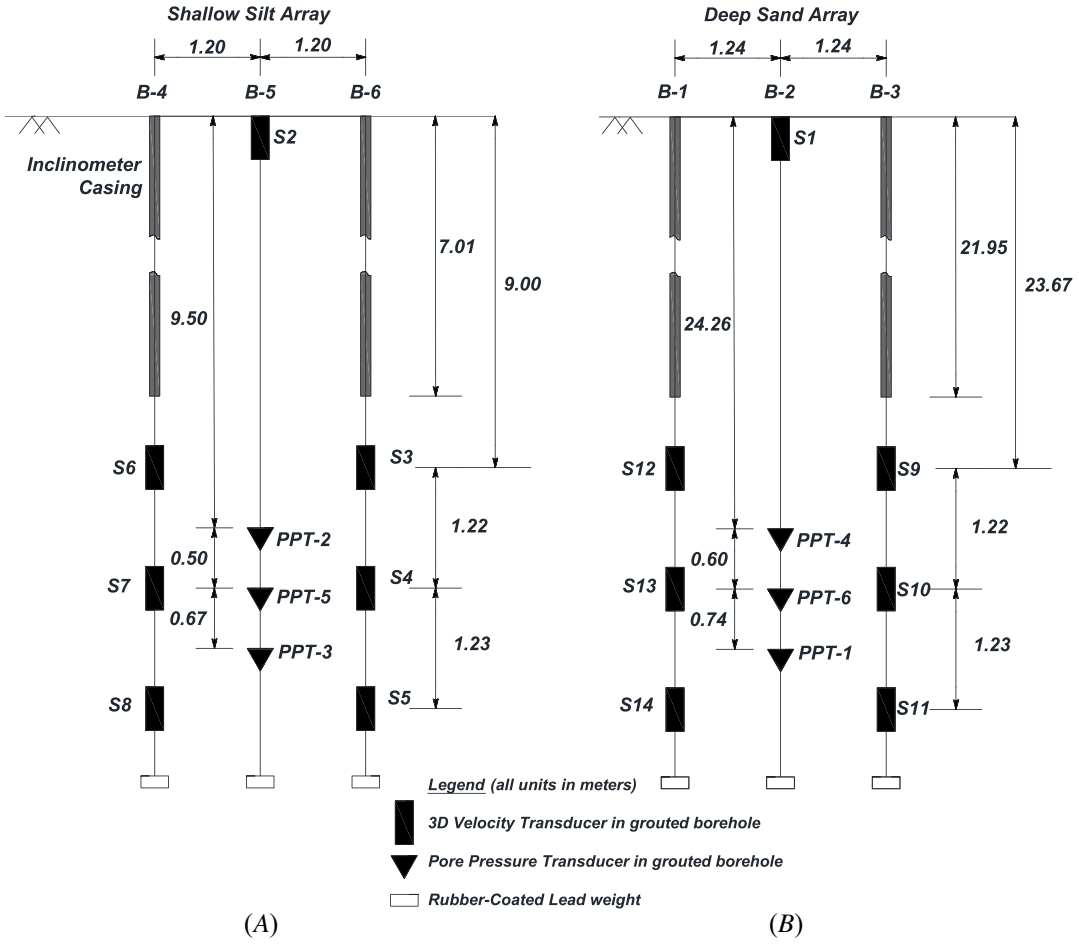

by Gianella and Stuedlein (2017) and was therefore selected for use in this study. The PPT can survive a blast pressure of 20.7 MPa, can reliably operate over the range of 0 to 5.2 MPa, and exhibits an accuracy of 0.04 % of full scale. The PPT can operate over a frequency of 1 to 3.5 kHz, appropriate for controlled blasting studies.

PPTs were installed within tremie-grouted boreholes following the procedures recommended by Mikkelsen and Green (2003). Each PPT was housed within an acrylic housing in order to help withstand the anticipated blast-induced hydrodynamic pore pressure and prevent intrusion of grout or foreign materials into the de-aired diaphragm chamber. In order to mitigate the potential for temporal lag and reduction in pressure amplitude between the hydrodynamic pore pressure and the measured electrical signal, two sintered, porous bronze filters were fixed to the housing at the location of the sensing diaphragm following procedures described in Cox, Stokoe, and Rathje (2009). Each PPT was calibrated within its acrylic housing prior to installation to ensure that the calibration would appropriately reflect the in situ pore pressures.

PPTs were calibrated within a water-filled inclinometer casing. Prior to calibration, the bronze filters were boiled for 10 min and secured to the housing under water. Air entrapped between the threaded tip of the PPT and the sensing diaphragm was removed prior to placement within the housing. The PPT and the housing were transferred to the calibration casing following placement of a latex membrane on the housing under water, which served to prevent loss of water through the filters during transfer. Each PPT was lowered to the bottom of the

casing and the depth noted, and corresponding excitation voltage sensed by the PPT was recorded at a sampling rate of 50 Hz for 30 s. Thereafter, the PPT was raised in 1.5-m and 30-s increments and the corresponding voltage signal observed. **Figure 4** presents the voltage time history for PPT 3 as an example, indicating noise typical of 100 % gain, applied during calibration owing to the potential magnitudes of pore pressures anticipated. Each PPT exhibited a unique voltage-pressure response, developed using the average measured excitation voltage at each observation depth/pressure head, and characterized with $R^2 > 0.999$ for each calibration curve, where R^2 is the coefficient of determination. **Figure 4*B*** indicates the need for individual calibrations (e.g., significantly nonzero intercepts) and deviation from the manufacturer supplied calibration record, which was disregarded.

CALIBRATION AND PREPARATION OF TGPs

TGPs were designed and fabricated to monitor the body wave and particle velocity necessary to determine the linear and nonlinear dynamic properties of the soil during geophysical and controlled blasting tests. Each TGP consisted of three orthogonally oriented geophones and one six degree-of-freedom inertial measurement unit (IMU). The geophones selected for use were Geospace Technologies Model GS-14-L9 with a natural frequency of 28 Hz and open circuit damping of 31 %. The geophone coil resistance and the open circuit sensitivity was 1,500 Ω and 23.62 V/m/s, respectively.

Each geophone was independently calibrated to develop its unique sensitivity curve, which relates the voltage to the particle velocity for a given excitation frequency. The calibration setup consisted of a MEMS accelerometer, a signal generator, oscilloscope, amplifier, electromagnetic shaker (i.e., a speaker driver), and a data acquisition system (**fig. 5*A***). A given geophone and MEMS accelerometer was fixed to the electromagnetic shaker and subjected to sinusoids generated between 10 and 300 Hz and the corresponding output signal was observed. Clear waveforms were achieved by varying the amplitude of the sinusoidal signal until satisfactory signal-to-noise ratios were identified. In general, the shape of the unique sensitivity curve developed for each geophone follows the standard, model-specific sensitivity curve provided by the manufacturer for frequencies below ~160 Hz (**fig. 5*E***). However, close inspection of **figure 5*E*** in this range indicates significant frequency-dependent deviations between the unique and standard sensitivity curves, particularly near the geophone natural frequency (i.e., 28 Hz); thus, unique, individual curves were used to compute the corresponding particle velocity. The standard sensitivity curve was invoked for frequencies greater than 150 Hz owing to limitations of the calibration equipment.

Each TGP was accompanied by an IMU to observe the as-built tilt of the TGP following placement within the grouted borehole. The IMU, consisting of Model GY-521 MPU-6050 (InvenSense 2013) is a six degree of freedom sensor that is capable of measuring static and dynamic acceleration in three orthogonal directions and rotations

FIG. 4 Pore pressure transducer calibration, including: (*A*) voltage time history for PPT 3 (full 10-V gain used as applied in the field), and (*B*) voltage to hydrostatic pressure relationships indicating PPT-specific responses.

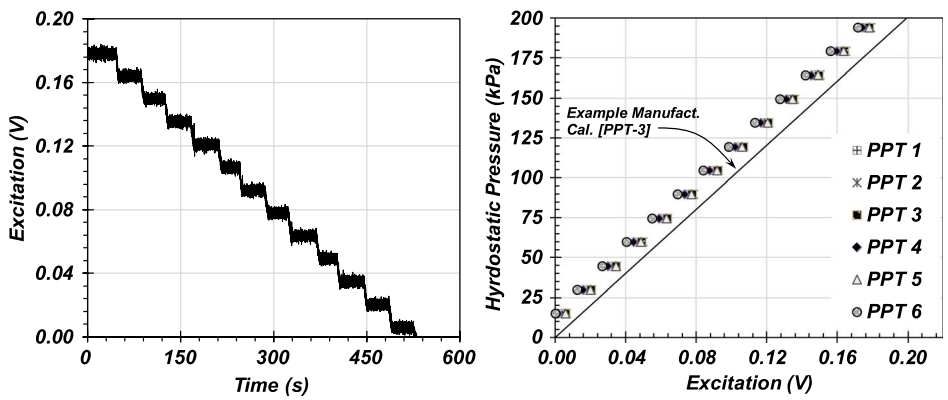

FIG. 5 Triaxial geophone package calibration and fabrication: (*A*) geophone and MEMS calibration setup, (*B*) acrylic housing with weighted geophone frame, MEMS, and IMU prior to placement of epoxy, (*C*) geophone frame housing with MEMS and IMU prior to placement, (*D*) completed geophone sensor package, and (*E*) comparison of observed geophone sensitivity curves to manufacturer-supplied sensitivity curve.

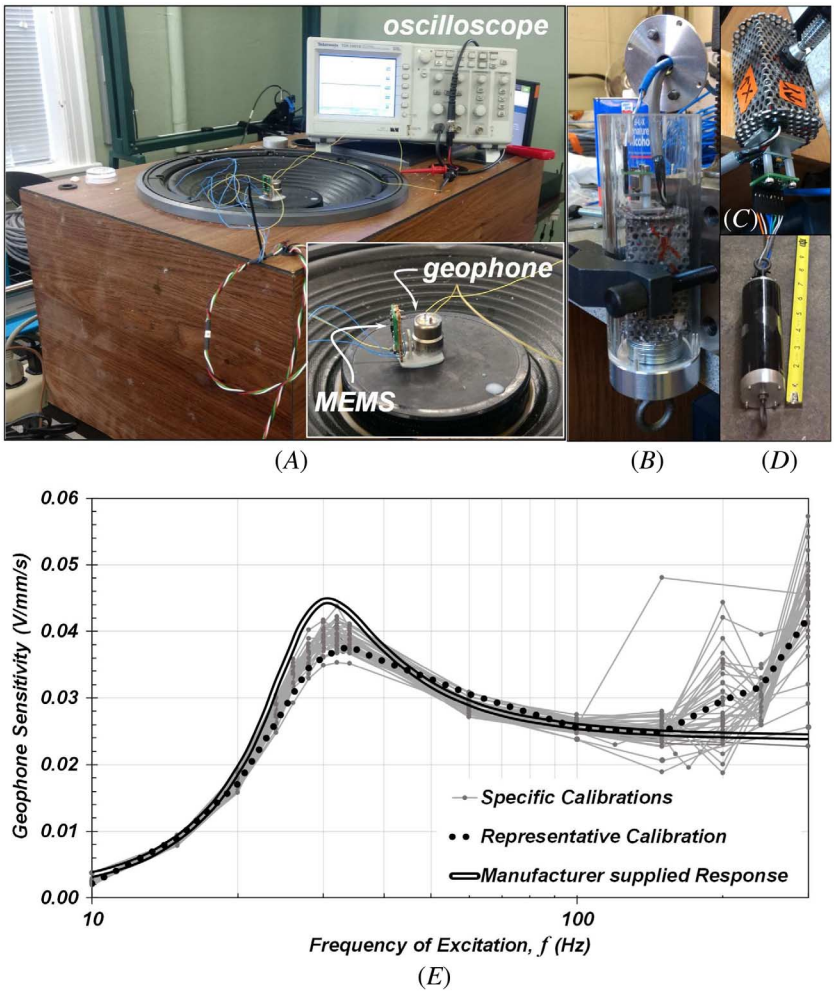

about three orthogonal directions. The MEMS triaxial accelerometer that is present in the IMU has a sensitivity of +/−16*g*, whereas the triaxial gyroscope can measure rotation up to 2,000°/s (InvenSense 2013). Each IMU was calibrated to define the baseline accelerometer using a triaxial tilt apparatus and noting the excitation voltage corresponding to true vertical, horizontal, and intermediate angles.

After calibration of the geophones and IMUs, the instruments were fixed to a perforated, steel, rectangular mesh cage (**fig. 5C**) and secured within an epoxy-filled, cylindrical, acrylic housing to ensure monolithic behavior. The length, inner, and outer diameter of the housing were 152, 51, and 64 mm, respectively. The housing was sized, along with aluminum bottom and top caps, and steel weights were added to achieve a total unit weight comparable to the soils investigated (i.e., about 18 kN/m^3). The bottom cap included a steel eyehook to allow suspension of lead weights or TGPs to form a single, self-plumbing multi-instrument string suspended from the base of inclinometer casing. Use of a single, multi-instrument string, achieved using steel cable, ensured that the vertical separation distance between geophones could be guaranteed while simultaneously providing sufficient

TABLE 1
Baseline gravitational excitation for first MEMS of each inclinometer module

	Inclinometer Module							
Module	1,029	1,030	1,031	1,032	1,124	1,125	1,126	1,127
Mean, g	0.624	0.632	0.636	0.602	0.623	0.631	0.616	0.615
Standard deviation, g	3.0×10^{-4}	2.7×10^{-5}	1.7×10^{-5}	5.4×10^{-3}	1.5×10^{-4}	5.4×10^{-4}	3.1×10^{-5}	7.8×10^{-4}
COV, %	0.047	0.004	0.003	0.899	0.023	0.086	0.005	0.127

slack to the communications cabling. The top cap included two steel eyehooks and an annular stem with a 13-mm inner diameter to allow passage of the cabling and strain relief measures. Instruments were directly fixed to the steel mesh, which was centered and plumbed prior to injecting the nonpolar epoxy and vibrated to minimize entrapped air as the epoxy flowed through the perforated cage housing while monitoring sensor output to provide an indication of integrity and plumbness during epoxying.

INCLINOMETER CALIBRATION FOR BOREHOLE DEVIATION SURVEY

The downhole and crosshole body wave velocities used to compute V_s rely upon accurate estimates of the vertical and horizontal separation distance, respectively, between geophones (ASTM D4428/D4428M-14, *Standard Test Methods for Crosshole Seismic Testing*; ASTM D7400/D7400M-19, *Standard Test Methods for Downhole Seismic Testing*; Cox et al. 2019). Whereas the depths and vertical separation distance of the TGPs could be specified, the accurate measurement of the lateral separation distance required careful observation of borehole deviation observed using inclinometers. Accordingly, the MEMS-based Geodaq i6 (Geodaq 2014) in-place inclinometer was used to observe the anticipated out-of-plumb borehole deviation. Two types of interchangeable MEMS inclinometer modules were used to survey each cased borehole: the INC6-R24, fitted with four dual-axis MEMS accelerometers, and the INC6-R28 with eight MEMS accelerometers spaced equally over the 2.44-m length of each module. Each accelerometer is capable of measuring the angular deviation from the vertical in two orthogonal directions within 0.004° and for inclinations up to 30° (Geodaq 2014).

In general, inclinometers are used for change-detection in tilt for applications such as slope stability, excavation-induced ground movements, and lateral loading tests of deep foundations, and the baseline initial tilt profile is largely irrelevant if within typical instrument limitations. For the present application to quantify borehole deviation, the inherent electro, mechanical, and thermo-mechanical noise (i.e., baseline error in the true vertical) of each MEMS sensor was of significance. In order to quantify the true zero-tilt baseline MEMS acceleration, a calibration frame of 4.89-m height was constructed and fitted with inclinometer casing, which passed through ten centering boxes. These boxes enabled plumbing of the casing. Each in-place inclinometer module was lowered within the plumbed casing, and the baseline signal registered in each MEMS were recorded by using the Geodaq microcontroller module (GCM4; ver. 4) at a frequency of 10 Hz to enable statistical characterization of the baseline acceleration. The registered signal was averaged over a 30-s period and repeated four times to establish a reliable baseline acceleration for each MEMS. Table 1 summarizes the mean, standard deviation, and coefficient of variation in acceleration for an example MEMS in each inclinometer module, indicating a relatively low, though unique, module-specific baseline acceleration representing their inherent electro-, mechanical, and thermomechanical noise. The mean baseline gravity of each MEMS was used to identify the actual deviation of the inclinometer casing within the borehole, described below.

Field Installation and Baseline Testing Protocols

INSTRUMENT INSTALLATION PROCEDURES

Each instrument string and casing was installed within 200-mm-diameter mud-rotary boreholes to form the two instrumented soil arrays used to capture the static and dynamic soil response. Prior to installation, the string of

three PPTs (per array) was formed using steel cabling at specified separation distances and a rubber-coated lead weight to assist with placement and plumbing within the heavy drilling mud-filled borehole. Before installation, the saturation procedures used during calibration were performed and maintained using latex membranes, the latter of which were removed incrementally below the drilling fluid level as the string was lowered into the borehole. Upon placement to the required depth, a lean, low-strength cement-bentonite grout was mixed following recommendations by Mikkelsen and Green (2003) and tremied to the base of the borehole to displace the drilling fluid and secure the PPTs to the surrounding soil. The two PPT strings were placed within boreholes B-2 (sand array) and B-5 (silt array; **fig. 1**) at the depths shown in **figure 3**.

Four strings of three TGPs were installed within boreholes B1 and B3 (i.e., the sand array) and B4 and B6 (within the silt array). Each weighted TGP string was formed using steel wire cable and suspended from the bottom of an inclinometer casing and grouted in place at the desired depth. The flexible steel cabling allowed the grouted TGP to respond individually to incoming body waves while ensuring that the vertical separation distance could be known with certainty, whereas the inclinometer casing would ensure knowledge of the borehole deviation up to the point where the TGPs could self-plumb within the borehole. Two additional, full-depth inclinometer casings fitted with corrugated plastic pipe and steel sondex sensing rings were grouted within boreholes I-1 and I-2 in order to quantify local settlements and vertical strain, as well as to document the borehole deviation within the soils at the same depth as the other instrumentation.

DETERMINATION OF THE IN SITU LOCATIONS OF THE TGPs

Efforts to determine the true location of the TGPs were undertaken approximately one month after installation of the sensors and curing of the grout. The full-depth in-place inclinometer was lowered to the bottom of each inclinometer casing and the static gravity in each inclinometer module was recorded. The gravitational shift in the measured static gravity was compared to the baseline static gravity of each MEMS and the cumulative sum of the individual tilt readings from the ground surface were used to compute the borehole deviation (Wilson and Mikkelsen 1977; Machan and Bennett 2008). **Figure 6*A*** presents the computed deviation of the inclinometer casing with respect to local coordinates (*X, Y*), referenced to the orientation of the grooves in the casing, whereas compass readings of the grooves enabled determination of the azimuthal orientation of the borehole deviation (**fig. 6*B***) and facilitated comparison to the linear blast array (**fig. 1**). **Figure 6*A*** and **6*B*** indicate a range in borehole deviations among the six borings, confirming the need to document the deviation of each borehole as prescribed by ASTM D4428/D4428M-14 and given the sensitivity of body wave

FIG. 6 Deviation of inclinometer cased mud-rotary borings drilled to house various instruments: (*A*) lateral deviation beginning from the ground surface relative to the local azimuthal reference system, and (*B*) plan view representation of deviation relative to the global azimuthal reference system.

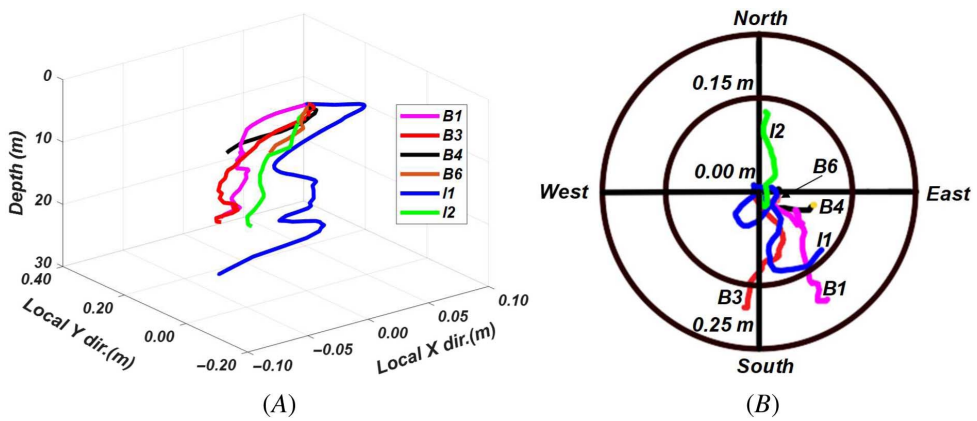

velocity to the distance between the receivers. The maximum observed borehole deviation was approximately 200 mm, approximately equal to the diameter of the tri-cone drill bit used. Thus, in the absence of the borehole deviation surveys and for the V_s of the silt deposit (equal to about 126 m/s), deviations of 0 to 200 mm in two adjacent boreholes would lead to errors in V_s ranging from 0 to 20 % for the intended lateral distance of the TGPs.

Each string of TGPs was suspended from the bottom of the inclinometer casing and allowed to self-plumb under gravity with the aid of the lead weight. Based on the measured static tilt angle observed using the IMU in each TGP (Table 2), the TGPs were nearly plumb. The lateral separation distance between laterally-adjacent TGPs could therefore be assumed constant and equal to the separation distance of the base of the adjacent inclinometers, determined using at-grade separation distances between the casings and measurements of the borehole deviation. The position with respect to the global east-west blast array alignment of each laterally-adjacent TGP pair and lateral separation distance is presented in Table 2, and was used to compute the shear strain and body wave velocity in the two arrays.

DETERMINATION OF ORIENTATION OF THE TGPs

The orientation of each TGP was unknown following installation; thus, downhole geophysical tests were necessary to determine the orientation of each geophone and its polarity. The in situ orientation of geophones can be determined using such methods as cross correlation (Zeng and McMechan 2006; Zha, Webb, and Menke 2013; Grigoli et al. 2012), polarization analysis (Jurkevics 1988; Zeng and McMechan 2006), particle motion analysis (Tréhu 1984), or a novel root mean squared error analysis developed as part of this study (Donaldson 2019). The latter two approaches were selected to determine the orientation of each geophone relative to the global east-west blast-array alignment.

Particle Motion Traces

The orientation of a given TGP can be determined by inspection of the particle motion in each component of the geophone when the body wave traverses through it (Tréhu 1984). Thus, varying the location of the downhole energy source relative to the TGP can allow changes in particle motion amplitude to be documented. A downhole test array consisting of a semicircle centered between two instrumented boreholes (e.g., B-4 and B-6; fig. 7) provided a convenient means to evaluate the sensitivity of particle motion amplitude with position. The radius

TABLE 2

Offset, angular tilt, and location of each TGP for the silt and sand arrays

TGP Pair	Separated E-W Distance, m	Offset in N-S [N$^+$], m	Offset in E-W [E$^+$], m	Depth, Z, below Ground Surface [Z$^+$], m	Tilt Angle in the X, °	Tilt Angle in the Y, °
			Silt Array			
B-4: S6	2.395	−0.013	0.110	8.991	2.18	2.58
B-6: S3		0.027	0.037	9.003	−0.6	−2.4
B-4: S7	2.395	−0.009	0.126	10.215	−2.9	−0.2
B-6: S4		0.045	0.042	10.223	−1.5	1.9
B-4: S8	2.395	−0.005	0.141	11.440	−1.9	−0.1
B-6: S5		0.060	0.047	11.451	−1.9	0.6
			Sand Array			
B-1: S12	2.484	−0.175	0.125	23.672	0.8	−0.1
B-3: S9		−0.226	−0.037	23.661	NA	NA
B-1: S13	2.484	−0.177	0.135	24.891	NA	NA
B-3: S10		−0.245	−0.039	24.882	−3.5	−3.4
B-1: S14	2.484	−0.180	0.142	26.113	−3.5	−1.6
B-3: S11		−0.264	−0.043	26.111	NA	NA

Note: NA = not available.

FIG. 7 Downhole test array to determine the orientation of TGPs comprising the shallow silt array with a radius of 7.62 m with shots (enumerated 1–25) spaced at approximately 1.07 m increments.

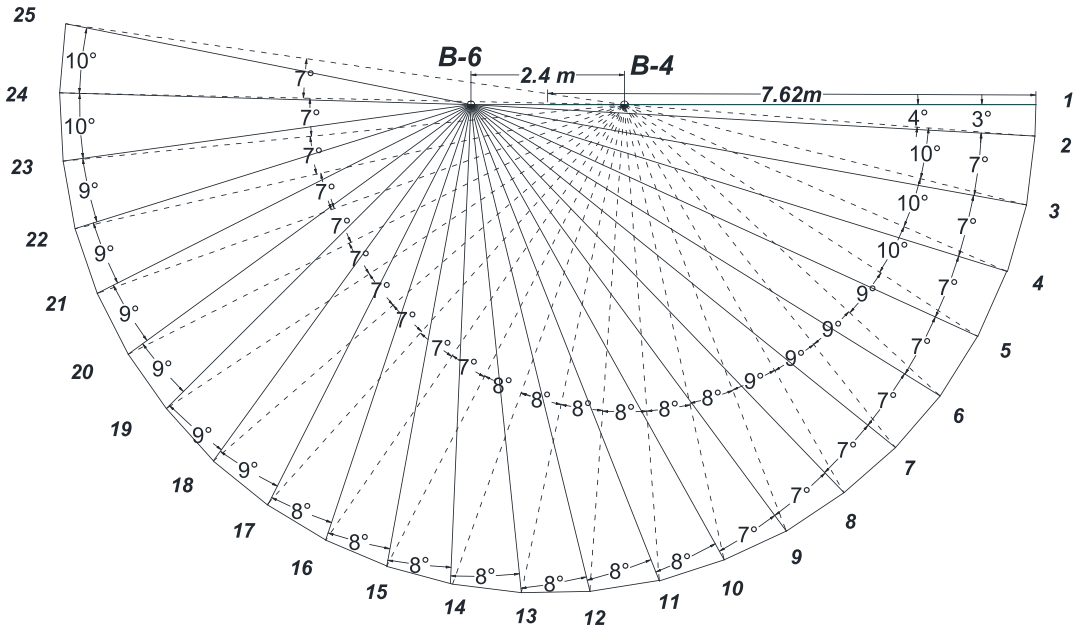

of the semicircle was chosen based on the body wave type used to analyze the particle motion and the wavelength generated. For example, the energy source should be located at least one full wavelength away from the TGP to generate a clear signal with proper distinction between compression and shear wave (Jurkevics 1988). Compression wave-dominant motions were generated by striking an aluminum plate, whereas vertically propagating horizontally polarized *SH*-waves were generated by striking the side of an embedded shear beam. Sledgehammers weighing 3.63 and 7.25 kg were alternately used to generate the signals depending on distance from the TGPs and degree of coupling of the plate and beam obtained, as judged from signal quality. Generally, the first and strongest sinusoid of the imposed body wave was selected to plot and identify the dominant direction relative to the known shot locations. **Figure 8** presents examples of the registered particle motions in the local *XY* (horizontal), *XZ* (vertical), and *YZ* (vertical) planes indicating the minimum and maximum amplitudes in two mutually perpendicular planes, providing a visual indication of the geophone orientations through registration of "strong" and "weak" particle motions in a given plane (Tréhu 1984). Once the generally predominant plane orientations were identified, additional neighboring shots were taken to improve the resolution of the geophone component directions. In general, compression waves were used to identify the orientation of the shallow TGPs and shear waves used to identify the orientation of the deep TGPs owing to the differing refractive and attenuation qualities of the body waves in layered strata. The particle motion plots corresponding to shots 2 and 14 for TGP S3 indicates that these locations correspond to mutually perpendicular planes.

Root Mean Square Error Analysis

A more quantitative approach to determine the absolute orientation of each geophone component direction is to compute the resultant vector motion amplitude of a given shot using a single dominant cycle of the measured waveform for two (near-perpendicular) geophone components (Donaldson 2019). Each geophone component amplitude was subtracted from the computed resultant vector, R_T, multiplied by the sum of the cosine angle of the shot, θ, and the proposed angle of deviation, i, referenced to the global east-west blast array alignment.

FIG. 8 Plots of particle motion for TGP S3 within borehole B-6, at orientations (shots 2 and 14; see **fig. 6**) that produced their maximum *X* and *Y* component amplitudes.

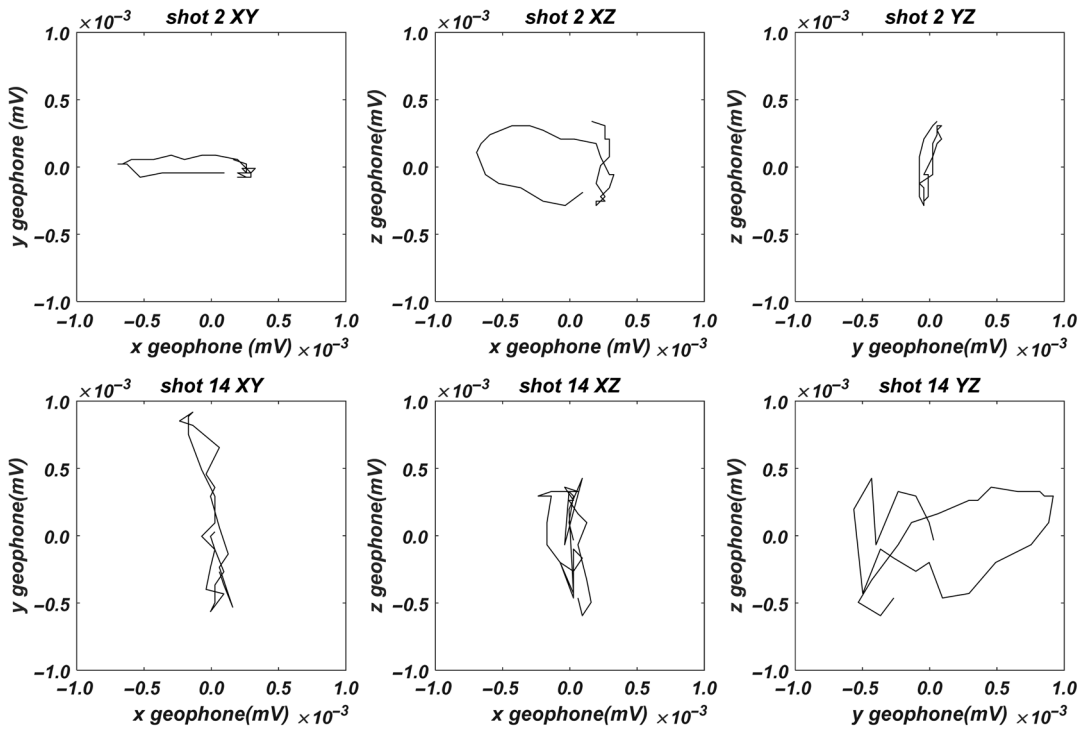

The root mean squared error (RMSE) of each nearly orthogonal geophone component is then computed using

$$RMSE(i) = \sqrt{\sum_{t=1}^{T} \frac{((R_T \cos(\theta + i) - x_t)^2}{T}} \quad (1)$$

where T is the number of discrete data points taken from one cycle of the dominant waveform, and x_t is the registered raw excitation voltage time history. An example of the RMSE for every shot plotted against i for TGP S3 is shown in **figure 9**. The angle of deviation from the east-west global alignment corresponding to the minimum RMSE value indicates the orientation of the sensor packages relative to due east or west.

Comparison of Methods and Finalization of TGP Orientation

Table 3 presents the orientation of each TGP referenced to the global east-west blast array alignment deduced using the particle motion trace and RMSE methods. The orientation of the *X* and *Y* geophone components for TGP S3 is 3° and 92° from due west (set equal to 0° prior to correcting for polarity) as deduced using the particle motion traces, whereas orientations of 9° and 96° were determined using the RMSE approach. The two methods produced similar angles for the same geophone packages, although some differences were noted as being due to differences in the accuracy of the methods and the inherent deviation from 90° due to imperfections in the fabrication of the TGPs. The RMSE approach was considered the most robust and reliable approach for the evaluation of orientation and so the orientations thus obtained were used, following slight adjustment for observed manufacturing deviations from 90°, in subsequent analyses of geophysical and controlled blasting tests. Following

FIG. 9

Root mean square error analysis for geophone sensor package, TPG S3, located in Boring B6. The orientations of the *X* and *Y* components correspond to the minimum RMSEs.

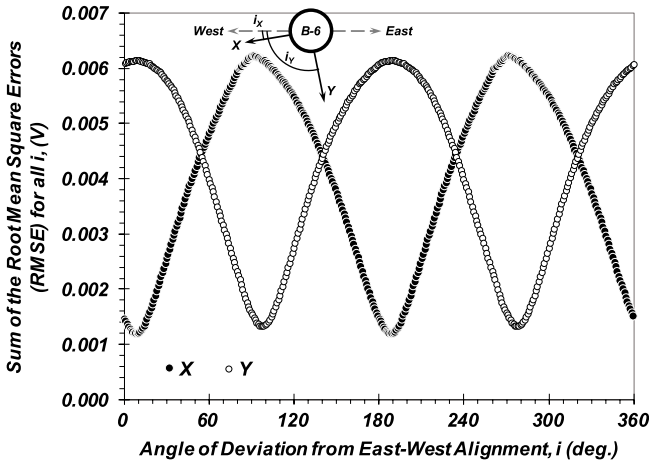

TABLE 3

Orientation of the TGPs from due west

TGP#	Boring	Particle Motion *x*, °	Particle Motion *y*, °	RMSE *x*, °	RMSE *y*, °	Polarity-Corrected Angle *x*, °	Polarity-Corrected Angle *y*, °
S3	B-6	3	92	9	96	6	94
S4	B-6	17	104	19	117	18	108
S5	B-6	65	149	61	154	63	152
S6	B-4	139	52	139	46	319	229
S7	B-4	132	44	134	43	313	224
S8	B-4	139	47	136	50	317	229
S9	B-3	130	43	141	48	136	46
S10	B-3	2	92	−2	89	0	91
S11	B-3	−1	92	−5	88	−3	90
S12	B-1	33	118	21	108	206	293
S13	B-1	15	102	5	96	10	99
S14	B-1	98	10	102	10	280	190

testing to determine the sensor orientation, the polarity of each geophone component was verified using the downhole methodology described by Cox et al. (2019) and the results of the controlled blast-induced crosshole data (described below). The final polarity-corrected orientations are shown in **Table 3**.

Example Results from an In Situ Controlled Blasting Test

The results from a test blast program, which was conducted to evaluate the site-specific ground motion attenuation relationships and impact to adjacent structures and buried utilities, make adjustments to the subsequent blast programs (not described herein), and to evaluate the operability and protocols for data acquisition, are used to demonstrate the ability to capture the inelastic, coupled fluid-mechanical response of the instrumented plastic silt array (**figs. 1*B*** and **3*A***). The test blast program consisted of eight charges varying from 227 to 3,628 g set within blast casing CX. This casing extended to a depth of 27.4 m and was located approximately 45 and 63.5 m from the center of the sand and silt arrays (**fig. 1*A***), respectively. The charges were detonated with 1-s delays to produce a 7-s velocity time history (**Table 4**) with waveforms unimpeded by superposition of multiple

TABLE 4
Charge weight, depths, and schedule of detonation comprising the test blast program

Detonation No.	Time, s	Depth, m	Charge Weight, *g*
1	0	6.6	227
2	1	8.2	454
3	2	10.2	907
4	3	12.6	1,814
5	4	18.2	454
6	5	20.2	907
7	6	22.6	1,814
8	7	25.7	3,628

detonations. The explosive charges consisted of unitronic electronic detonators and Pentex cast boosters, connected using a 48-grain detonating cord to form each specified charge. The manufacturer-specified velocity of the explosive was 7,900 m/s with detonation pressure of 240×10^5 kPa. Charges were lowered to the specified depth within the blast casing and gravel stemming used to separate charges and retain energy within the casing. The TGPs and PPTs were sampled at 10 kHz and acquired using a NI-DAQmx and LabVIEW acquisition system.

CHARACTERISTICS OF BLAST-INDUCED GROUND MOTIONS

The raw voltage excitation measured for each of the TGPs was filtered using a low pass, third-order Butterworth filter to remove very high frequency noise. The filter cutoff frequency of 1,500 Hz, higher than that typically used in earthquake ground motion applications, was selected to minimize the loss of the signal energy in the high-frequency waveforms (described below). Then the filtered signal was passed through the high pass filter with cutoff frequency of 1 Hz to minimize spurious amplification of low-amplitude–low-frequency signals during conversion of voltage to velocity in the frequency domain. Because of the need to supply frequency-dependent conversion factors, inspection and correction of each waveform was required to correct Fourier transform-induced errors.

Figure 10 presents an example of the three-component velocity time histories for TGP S6 observed during the test blast, including the three-component particle velocity record for the entire test blast program (fig. 10*A*) and the full blast waveform for blast #4 to illustrate differences in body waves (fig. 10*B*). Note that changes in the waveform between the source and the measurement are irrelevant for the purposes of quantifying the coupled fluid-mechanical response of the soil bounded by the silt array. The TGP orientations shown in Table 3 were used to correct the measured velocities to the east-west (TGP S6x) and north-south (TGP S6y) directions. The particle velocity and displacement from the far-field produces maximum ground motions in the vertical (*x*-*z*) plane as observed from the low amplitudes registered in TGP S6y. The initial, high-frequency particle velocities indicate the arrival of the blast-induced P-wave, immediately followed by local S-waves developed because of unloading of the P-wave, resulting in near-field shearing of the soil (Sánchez-Salinero, Roesset, and Stokoe 1986). The near-field S-wave, identified by its lower frequency content (fig. 10*C*), is followed by the arrival of the far-field S-wave generated at the location of the charge (fig. 10*B* and 10*C*).The detonation source-to-sensor distance, compressive wave velocity of the soil (approximately $V_p =$ 940 m/s), and initial crosshole shear wave velocity ($V_s = 126$ m/s) of the soil were used to identify the shear wave arrival, which was evaluated in consideration of the normalized Stockwell spectrogram (fig. 10*C*) constructed using the longitudinal (6x) velocity time history following the procedures described by Kramer, Sideras, and Greenfield (2016). For the case of blast #4, the far-field S-wave (more clearly delineated in the particle displacements shown in fig. 10*D*) arrived somewhat earlier than expected, perhaps owing to variability in V_s between the charge and array and location of the charge at the interface of the plastic silt and underlying medium dense sand layer, the latter of which was characterized by a higher V_s.

FIG. 10 Example velocity time histories observed during the test blast program: (*A*) three-component velocity time history for TGP S6 over the 7-s blast event, and details for blast #4 including (*B*) three-component velocity time history indicating the P-wave arrival, near-field S-waves that are due to local shearing associated with unloading of the P-wave, and far-field S-wave generated at the source; (*C*) normalized Stockwell spectrogram illustrating the time-varying frequency content of velocity in the longitudinal (east-west) direction; and (*D*) three-component displacement time history.

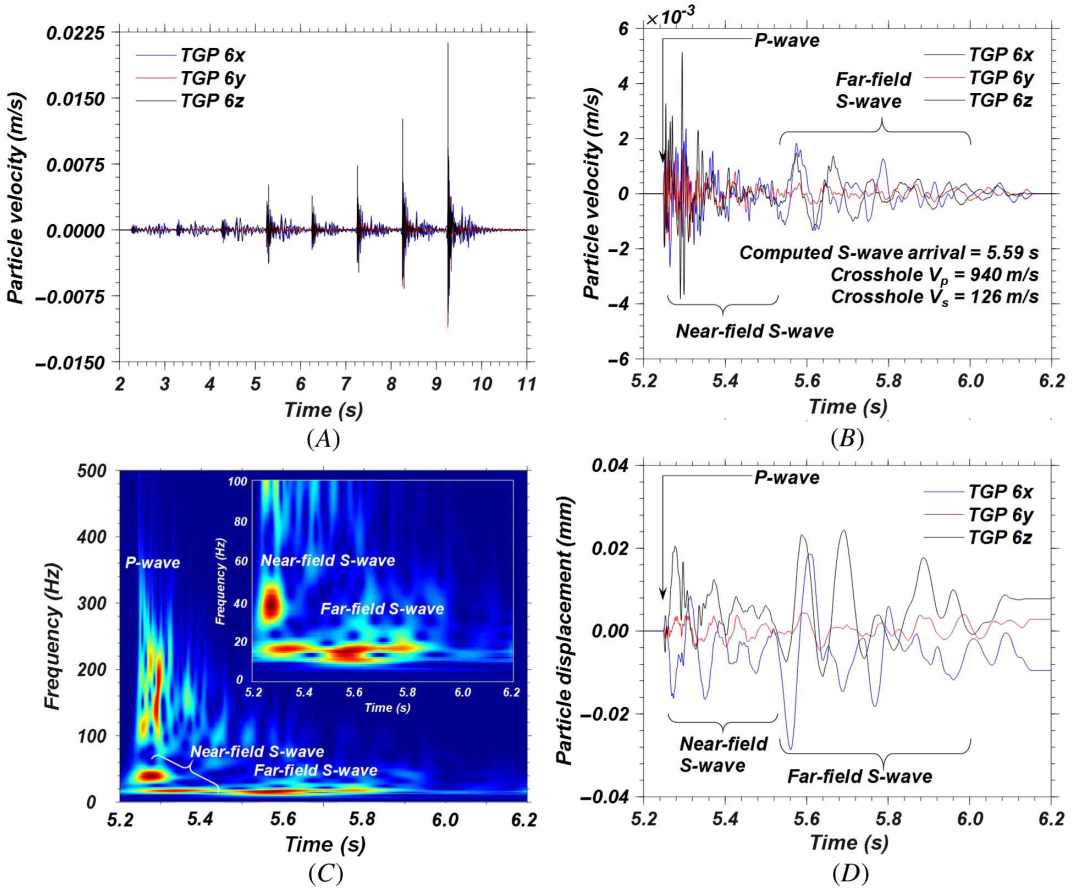

The predominant frequencies, f, of the blast-induced P-wave and near-field S-wave ranged from 100 to 250 Hz and 15 to 35 Hz, respectively (fig. 10*C*). The normalized Stockwell spectrogram indicates a clear separation between the near-field and far-field S-waves in time, with f ranging from 13 to 18 Hz. The particle displacements for blast #4 and shown in figure 10*D* indicates that the maximum P-wave particle displacements ($D_x = 0.004$, $D_y = 0.002$, and $D_z = 0.005$ mm) are significantly smaller than the near-field ($D_x = 0.016$, $D_y = 0.004$, $D_z = 0.020$ mm) and far-field ($D_x = 0.028$, $D_y = 0.004$, $D_z = 0.024$ mm) -induced shear waves. The low P-wave displacement amplitudes result in small contributions to shear strain upon unloading, with the largest components of shear strain being due to the near- and far-field S-waves as described below.

The wavelength, $\lambda = V_s/f$ (Kramer 1996), of the S-waves varied slightly throughout the test blast program. For example, the wavelength associated with the far-field S-wave shown in figure 9*B* for blast #4 was about 7 m, whereas $\lambda = 8.3$ m for blast #8. These wavelengths sample larger volumes of soil than the smaller wavelengths associated with typical high-frequency, small-strain downhole geophysical tests, and are more comparable to the wavelengths associated with earthquake ground motions.

CALCULATION OF TWO-DIMENSIONAL SHEAR STRAIN

The displacement time histories at the TGPs can be used to determine shear strain by setting the TGP locations equal to equivalent "nodes" in a finite element mesh (Rathje, Chang, and Stokoe 2005; Chang et al. 2007; Cox, Stokoe, and Rathje 2009; Stokoe et al. 2014; Sahadewa et al. 2015; Roberts et al. 2016, 2017; Zhang, Stokoe, and Menq 2019). The particle velocities observed in each TGP were integrated numerically (using the trapezoid rule) to obtain the corresponding displacement time histories as shown in **figure 10*D***. Thereafter, the computed displacement time histories were corrected for baseline drift using typical procedures (e.g., Boore, Stephens, and Joyner 2002; Boore 2005). The six TGPs were used to form two rectangular finite elements, designated elements 1 and 2, consisting of TGPs S3, 4, 7, and 6, and TGPs S4, 5, 8, and 7, respectively (**fig. 3*A***). Thereafter, the physical nodal locations are mapped to a unit coordinate plane and appropriate shape functions used to compute the shear strain at the location of each element-centered PPT. **Figure 11*A*** presents the computed shear strain time history for the two finite elements with the corresponding excess pore pressure responses presented in **figure 11*B***. At the end of the test blast, the residual excess pore pressure ratios, r_u, defined as the ratio of pore pressure in excess of hydrostatic and the initial vertical effective stress, for elements 1 and 2, were 0.35 % and 0.77 %, respectively, corresponding to peak shear strain magnitudes of 0.0118 % and 0.0072 %, respectively. The results from the test blast indicates that blast #8 induced shear strains that have exceeded the threshold shear strain for excess pore pressure development, γ_{tp}, in the silt.

Figure 12 presents the shear strain time histories for selected blasts as computed for the two elements, indicating that a change in the constitutive response of the soil occurred over the duration of the blast, transitioning

FIG. 11

Comparison of the (*A*) calculated shear strain time history in the shallow silt array for elements 1 and 2, and (*B*) measured excess pore pressure ratio time history for PPTs 2 and 3.

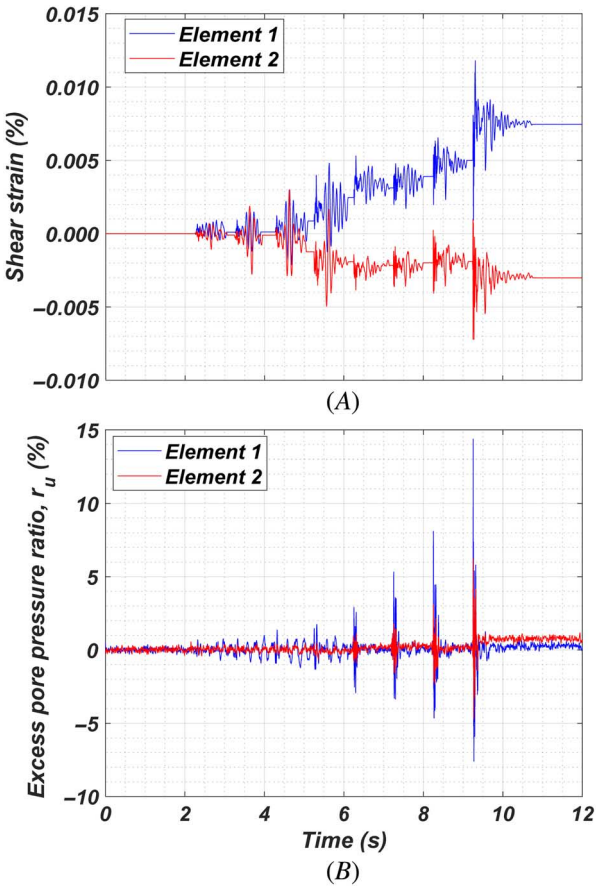

FIG. 12 Examples of shear strain time histories for the 8-s blast sequence in the shallow silt array. Note changing scale on the ordinate across figures.

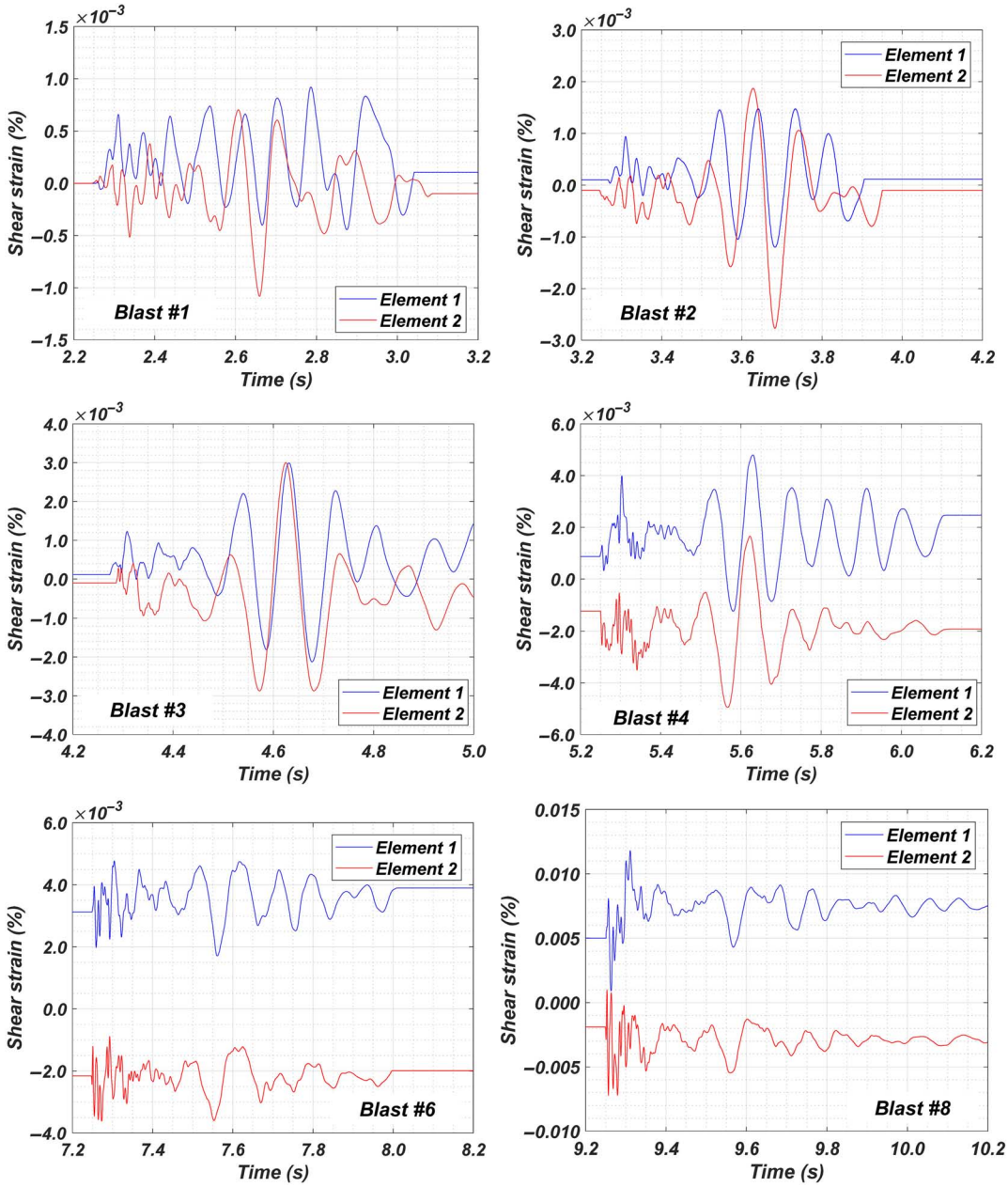

from linear-elastic to nonlinear-inelastic. For example, the first detonated charge produced a linear-elastic response in the silt array, but as blasting continued, the array accumulated permanent residual shear strains in the direction governed by the charge location-dependent ray paths emanating toward the element locations. The peak shear strain corresponded to passage of the far-field *S*-wave for all of the blasts except the last and largest blast; in this case, the peak shear strain developed in response to the near-field S-wave. Thus, the ray path (i.e., the source-to-site distance and direction) and charge weight play a significant role in whether shear strains will be dominated

by near-field or far-field shear loading. Following the test blast sequence, the maximum residual shear strain in elements 1 and 2 were 0.0073 % and 0.0033 %, respectively.

RELATIONSHIP BETWEEN SHEAR MODULUS AND EXCESS PORE PRESSURE WITH DSS-EQUIVALENT SHEAR STRAIN

Extensive downhole testing and the crosshole velocities observed during the test blast program provide a benchmark for comparison of the in-blast shear modulus, *G*. Whereas the downhole tests provide the shear wave velocity for vertically propagating horizontal shear (*SH*) waves, the blast programs produced horizontally propagating vertical shear (*SV*) waves (**fig. 10**), and differences between the two may arise because of soil anisotropy, as discussed below.

Preblast Downhole (*SH*) Shear Wave Velocities

Downhole testing was performed in accordance with ASTM D7400/D7400M-19 prior to the blast program to establish the baseline shear wave velocity. **Table 5** presents the average *SH* V_s for various TGP pairs measured in the silt array prior to blasting. The average V_s ranged from 119 to 154 m/s for any given TGP pair, indicative of the variability observed with CPT-3; the difference noted in borehole B-4 may be attributed to a variable grout column diameter. A representative magnitude of V_s of 126 m/s appears appropriate. Calculation of shear strains using the ratio of particle and shear wave velocity confirmed that downhole testing produced motions in the linear-elastic range and may be used to establish the *SH* maximum shear modulus, $G_{max,SH}$.

In-blast Crosshole (*SV*) Shear Wave Velocities

The change in shear modulus with imposed shear strains may be deduced using the crosshole shear wave velocities observed during the blast programs. The crosshole shear wave velocity for each blast pulse was calculated based on the difference in arrival times observed in laterally offset TGPs and the computed ray path distance separating each charge and TGP. The governing ray path was assumed equal to the straight line distance between the center of each charge source (Heelan 1953) to each TGP. Depending on the ray path distance and orientation, and the length of the charge relative to the length of array, the blast-induced loading may be represented as a two-dimensional (2D) plane wave, for far-field conditions, and as a three-dimensional (3D) wave for near-field conditions. The governing wave field (i.e., 2D versus 3D) can be determined by comparing the particle velocity time histories of two vertical (or "*z*") components of TGPs located within the same borehole. Such a comparison is provided in **figure 13*A*** and **13*B*** for measurements during the test blast program, which indicates that the amplitudes and phase of the vertically polarized horizontal shear waves passing through the borehole at the array location are identical for the charge considered. Small differences between the waveforms may have resulted from slight differences in the orientations of the TGPs and interference from the grouted borehole column, which may exhibit variations in diameter and position with depth.

TABLE 5

Downhole shear wave velocities observed within the silt array for horizontal components closest to the global east-west blast array alignment determined using the interval method

TGP Pair	S3 and S4	S4 and S5	S3 and S5
Borehole	B-6	B-6	B-6
Range in depth, m	9.0 to 10.2	10.2 to 11.5	9.0 to 11.5
Average V_s, m/s	125	126	126
TGP Pair	S6 and S7	S7 and S8	S6 and S8
Borehole	B-4	B-4	B-4
Range in depth, m	9.0 to 10.2	10.2 to 11.4	9.0 to 11.2
Average V_s, m/s	119	154	136

FIG. 13 Comparison of particle velocities for two inline, vertically separated geophones located within the same borehole observed during blast #2 and blast #3: (*A*) TGPs 7 and 8 located within borehole B-4 and (*B*) TGPs 4 and 5 and located within borehole B-6 and determination of time delay between SV-waves for two horizontally separated geophones located within different boreholes during blast #2: (*C*) TGPs S3 and S6, and (*D*) TGPs S5 and S8.

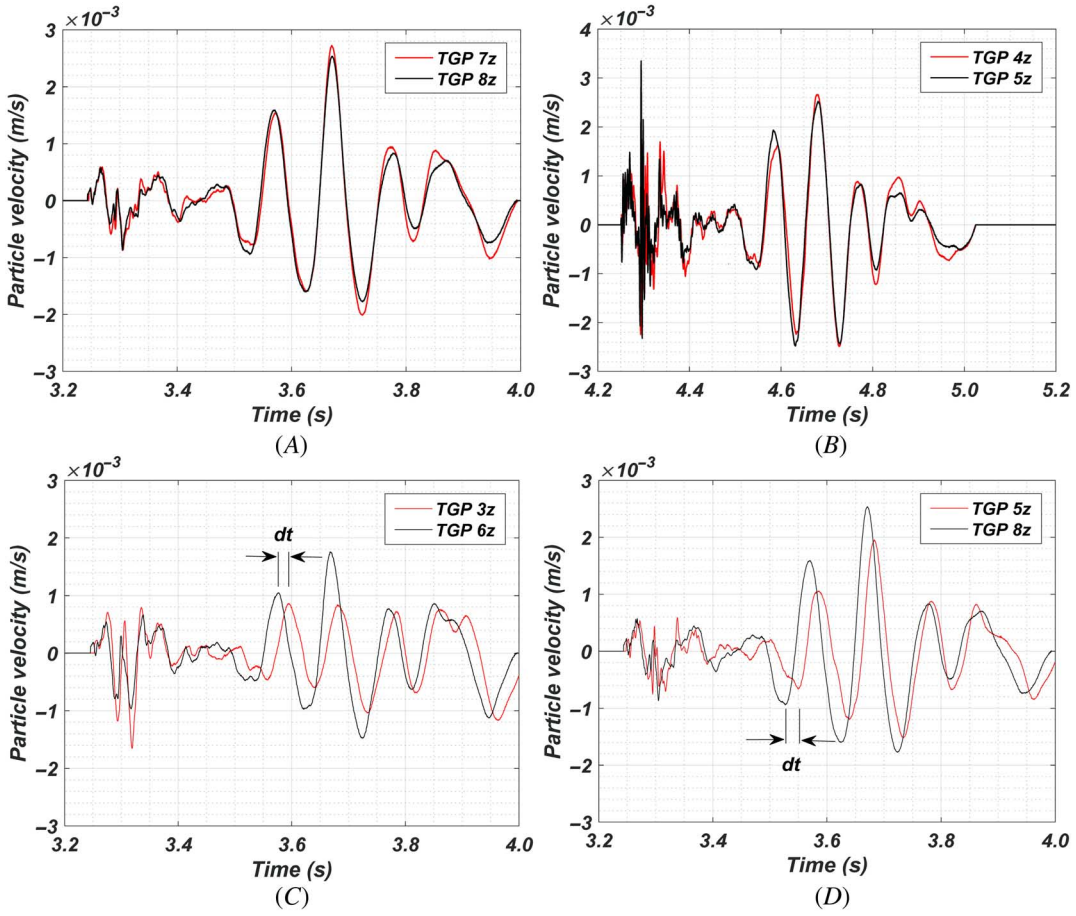

Calculation of DSS-Equivalent Shear Strain

The stress path arising from controlled blasting, dictated by the variables described previously, is different from typical cyclic laboratory tests often used to develop coupled fluid-mechanical relationships describing the dynamic response of soil. The cyclic direct simple shear (DSS) tests are preferred dynamic tests for geotechnical earthquake engineering because their stress path simulates vertically propagating horizontal shear waves. Figures 11 and 12 presented the shear strain component (γ_{xz}) of the 2D Cauchy strain tensor derived from the isoparametric finite element formulations; this approach also allowed calculation of the corresponding normal strain components ε_{xx} and ε_{zz}. To compare the mobilized in situ strain with the laboratory results from cyclic DSS tests, the deviatoric strain invariant or octahedral shear strain, γ_{oct}, is first computed from the 2D Cauchy strain tensor for plane strain (i.e., plane wave) conditions (Cappa, Brandenberg, and Lemnitzer 2017):

$$\gamma_{oct} = \left(\frac{2}{3}\right)\sqrt{(\varepsilon_{xx})^2 + (-\varepsilon_{zz})^2 + (\varepsilon_{zz} - \varepsilon_{xx})^2 + 6\left(\frac{\gamma_{xz}}{2}\right)^2} \quad (2)$$

FIG. 14

Octahedral shear strain time history for the silt deposit in the test blast program and 2D plane wave conditions (compare to **fig. 10*A***).

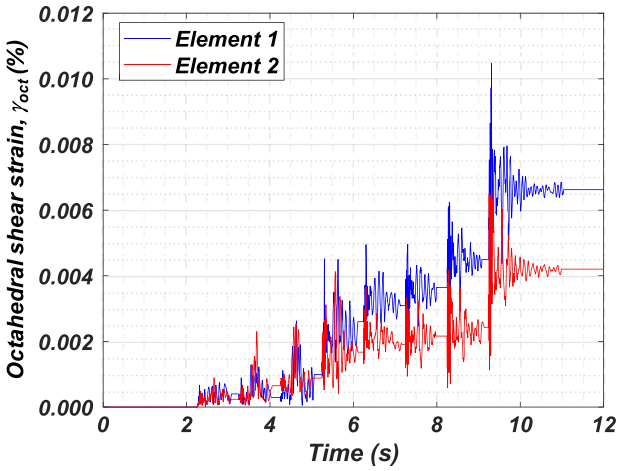

Figure 14 illustrates the octahedral shear strain time history for elements 1 and 2, indicating that the maximum absolute magnitudes of shear strain in these elements slightly reduced and increased, respectively, as a result of inclusion of the normal strains. Very little difference between the absolute magnitudes of shear strain early in the test blast program was noted. The constant-volume DSS-equivalent shear strain, $\gamma_{DSS,eq}$, representing undrained conditions (i.e., $\varepsilon_{xx} = \varepsilon_{zz} = 0$) was then scaled from γ_{oct} using (Cappa, Brandenberg, and Lemnitzer 2017)

$$\gamma_{DSS,eq} = \sqrt{\frac{3}{2}}\gamma_{oct} \tag{3}$$

for the comparison of shear modulus reduction to follow.

Determination of Shear Modulus versus DSS-Equivalent Shear Strain Relationship

The shear modulus of the silt within the silt array is computed from the crosshole *SV* shear wave velocities observed during the blast programs, which are in turn deduced from the difference in arrival time *dt* from laterally-separated TGPs (**fig. 13*C*** and **13*D***). **Figure 15*A*** presents the variation in shear wave velocity with 2D

FIG. 15 In situ, coupled, nonlinear inelastic response of plastic silt layer at a 10-m depth: (*A*) variation of shear wave velocity with 2D shear strain, and (*B*) variation of G/G_{max} and r_u with the maximum DSS-equivalent shear strain.

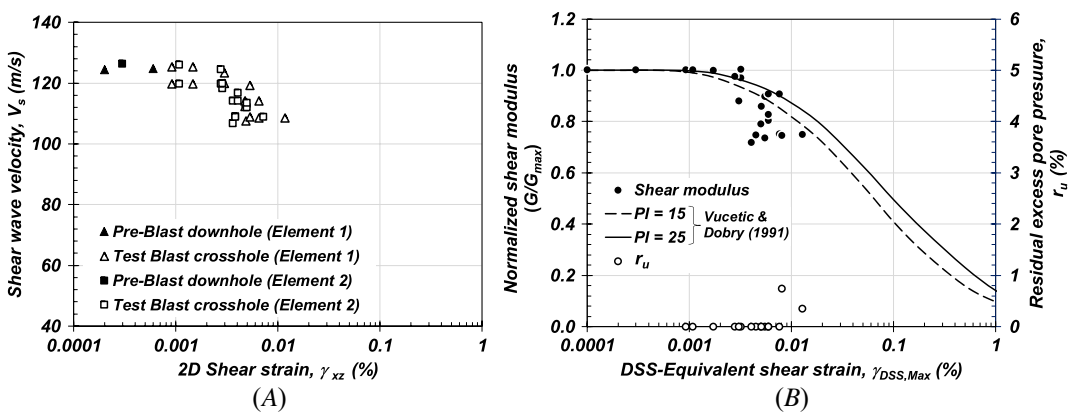

Cauchy shear strain; the plastic silt responded in a linear-elastic manner until $\gamma_{DSS} \approx \gamma_{xz} = \gamma_{te}$ of about 0.003 %, whereupon the soil begins to exhibit sufficient nonlinearity to degrade its wave propagation velocity by approximately 15 %. **Figure 15*A*** also shows that there is insufficient evidence to suggest significant soil anisotropy in the linear-elastic regime given the similarity in shear wave velocity between the preblast downhole and the initial blast-induced crosshole velocities.

The observed reduction in the shear wave velocity during the test blast program can be used to compute the shear modulus reduction in response to dynamic shear strains. The shear modulus, G, is computed using

$$G = \rho \cdot V_s^2 \tag{4}$$

where ρ is the density of the soil, set to a laboratory test-derived representative value of 1,580 kg/m^3. Elastic shear strains, such as those observed using downhole tests and the smaller charges in the test blast program, allow calculation of the representative G_{max} for elements 1 and 2, equal to 23 and 25 MPa, and 29 and 28 MPa, respectively. These magnitudes formed the basis for normalization of G and comparison to the corresponding maximum DSS-equivalent shear strain, presented in **figure 15*B***.

Figure 15*B* also plots the shear modulus reduction curve interpolated from the Vucetic and Dobry (1991) family of shear modulus reduction curves for plastic soils for representative *PI* of 15 and 25, along with the residual shear-induced r_u. Based on **figure 15*B***, it appears that the shear modulus must reduce to the range of approximately $0.71G_{max}$ to $0.74G_{max}$ in order to begin triggering the development of residual excess pore pressure, the maximum of which was 0.77 %. These results also suggest that $\gamma_{DSS} = \gamma_{tp}$ ranges between 0.008 and 0.013 % for the soil within the two elements. Given this magnitude of DSS-equivalent shear strain, little change in soil fabric following the test blast program was anticipated based on the cyclic laboratory test data reported by Hsu and Vucetic (2006).

Conclusions

The steps necessary to obtain the dynamic properties of soil under in situ conditions using controlled blasting were described in this study. Such an approach can be used in any soil, at any depth, provided the appropriate instrumentation and installation procedures are observed. Specifically, the elements deemed necessary and described herein included the following:

1. Calibration of the unique excitation voltage-to-unit relationships of each instrument (e.g., MEMS accelerometers, geophones, and PPTs) and the true baseline vertical acceleration of MEMS-based inclinometers. Manufacturer-provided calibration records were found to deviate from those observed in each instrument.
2. Surveying of the as-built geophone tilt and the deviation of drilled boreholes with inclinometers, with subsequent linkage to a global azimuthal reference in order to determine the crosshole separation distance necessary to compute body wave velocities.
3. Extensive downhole testing to determine the as-built orientation of the geophones using particle motion trace and a RMSE analysis. Whereas particle motion analyses provided approximate sensor orientations, the RMSE approach provided a more robust and reliable estimate of orientation.

Controlled blasting of various explosive charges was then used as the energy source to generate seismic body waves, which generated shear strains sufficient to exceed the nonlinear inelastic shear strain of a plastic silt deposit. Observations include that body waves can pass as plane waves (on the scale of the array implemented) and that the passage of *P*-waves results in shear strains upon unloading. Whether the near-field or far-field shear wave produced the largest shear strain component of given blast depended on the specific charge (i.e., size and length) and the ray path. Measured horizontally propagating vertically polarized shear wave velocities were used to construct the in situ relationship between shear modulus and maximum shear strain at a depth of approximately 10 m and to relate the reduction in stiffness with the corresponding excess pore pressure. Conversion of the calculated

2D Cauchy strain tensor to a constant-volume DSS-equivalent shear strain allowed direct comparison to commonly used shear modulus reduction curves. The novel controlled blasting experimental technique described herein demonstrated that coupled fluid-mechanical constitutive model parameters, such as the threshold shear strain to depart from linear-elastic and nonlinear elastic soil response, which is necessary for nonlinear site response and numerical deformation analyses, can be obtained in situ, at any depth, and in any soil that can be successfully drilled.

ACKNOWLEDGMENTS

The authors gratefully acknowledge the sponsors of this work: the Port of Portland, Portland, Oregon, and the Cascadia Lifelines Program and member agencies. The authors are particularly grateful to Tom Wharton, P.E. (OR), for his vision and oversight at the Port of Portland. Members of the research team were supported by the National Science Foundation (Grant CMMI-1663654) under the supervision of Dr. Richard Fragaszy, P.E., while conducting this work. Thanks are due to James Batti, Jeff Gent, Erick Moreno-Rangel, and Ali Dadashi of Oregon State University for their assistance during various portions of the field work. The authors are grateful for the care and diligence of Jerry Wallace, Wallace Technical Blasting, and for the insight provided by, and discussions with, Professors Kenneth H. Stokoe II, Brady R. Cox, and Anne Tréhu. Thanks are due to the anonymous reviewers for their helpful comments.

References

Amoroso, S., G. Milana, K. M. Rollins, C. Comina, L. Minarelli, M. R. Manuel, P. Monaco, et al. 2017. "The First Italian Blast-Induced Liquefaction Test (Mirabello, Emilia-Romagna, Italy): Description of the Experiment and Preliminary Results." *Annals of Geophysics* 60, no. 5: 1–19. https://doi.org/10.4401/ag-7415

Amoroso, S., K. M. Rollins, P. Andersen, G. Gottardi, L. Tonni, M. F. G. Martínez, K. Wissmann, et al. 2020. "Blast-Induced Liquefaction in Silty Sands for Full-Scale Testing of Ground Improvement Methods: Insights from a Multidisciplinary Study." *Engineering Geology* 265 (February): 105437. https://doi.org/10.1016/j.enggeo.2019.105437

Andrus, R. D., N. P. Mohanan, P. Piratheepan, B. S. Ellis, and T. L. Holzer. 2007. "Predicting Shear-Wave Velocity from Cone Penetration Resistance." Paper presented at Fourth International Conference on Earthquake Geotechnical Engineering, Thessaloniki, Greece, June 25–28, 2007.

Ashford, S. A., T. Juirnarongrit, T. Sugano, and M. Hamada. 2006. "Soil-Pile Response to Blast-Induced Lateral Spreading 1: Field Test." *Journal of Geotechnical and Geoenvironmental Engineering* 132, no. 2 (February): 152–162. https://doi.org/10.1061/(ASCE)1090-0241(2006)132:2(152)

ASTM International. 2014. *Standard Test Methods for Crosshole Seismic Testing*. ASTM D4428/D4428M-14. West Conshohocken, PA: ASTM International, approved March 1, 2014. https://doi.org/10.1520/D4428_D4428M-14

ASTM International. 2019. *Standard Test Methods for Downhole Seismic Testing*. ASTM D7400/D7400M-19. West Conshohocken, PA: ASTM International, approved Febuary 1, 2019. https://doi.org/10.1520/D7400_D7400M-19

Boore, M. 2005. "On Pads and Filters: Processing Strong-Motion Data." *Bulletin of the Seismological Society of America* 95, no. 2 (April): 745–750. https://doi.org/10.1785/0120040160

Boore, D. M., C. D. Stephens, and W. B. Joyner. 2002. "Comments on Baseline Correction of Digital Strong-Motion Data: Examples from the 1999 Hector Mine, California, Earthquake." *Bulletin of the Seismological Society of America* 92, no. 4 (May): 1543–1560. https://doi.org/10.1785/0120000926

Cappa, R., S. J. Brandenberg, and A. Lemnitzer. 2017. "Strains and Pore Pressures Generated During Cyclic Loading of Embankments on Organic Soil." *Journal of Geotechnical and Geoenvironmental Engineering* 143, no. 9 (September): 04017069. https://doi.org/10.1061/(ASCE)GT.1943-5606.0001721

Chang, W. J., E. M. Rathje, K. H. Stokoe II, and K. Hazirbaba. 2007. "In Situ Pore Pressure Generation Behavior of Liquefiable Sand." *Journal of Geotechnical and Geoenvironmental Engineering* 133, no. 8 (September): 921–931. https://doi.org/10.1061/(ASCE)1090-0241(2007)133:8(921)

Charlie, W. A., T. E. Bretz, L. A. Schure, and D. O. Doehring. 2013. "Blast-Induced Pore Pressure and Liquefaction of Saturated Sand." *Journal of Geotechnical and Geoenvironmental Engineering* 139, no. 8 (August): 1308–1319. https://doi.org/10.1061/(ASCE)GT.1943-5606.0000846

Charlie, W. A., P. J. Jacobs, and D. O. Doehring. 1992. "Blast Induced Liquefaction of an Alluvial Sand Deposit." *Geotechnical Testing Journal* 15, no. 1 (March): 14–23. https://doi.org/10.1520/GTJ10220J

Cox, B. R., K. H. Stokoe II, and E. M. Rathje. 2009. "An In-Situ Test Method for Evaluating the Coupled Pore Pressure Generation and Nonlinear Shear Modulus Behavior of Liquefiable Soils." *Geotechnical Testing Journal* 32, no. 1 (January): 11–21. https://doi.org/10.1520/GTJ101484

Cox, B. R., A. C. Stolte, K. H. Stokoe II, and L. M. Wotherspoon. 2019. "A Direct-Push Crosshole (DPCH) Test Method for the In Situ Evaluation of High-Resolution P- and S-Wave Velocities." *Geotechnical Testing Journal* 42, no. 5 (September): 1101–1132. https://doi.org/10.1520/GTJ20170382

Dahl, K. R., J. T. DeJong, R. W. Boulanger, R. Pyke, and D. Wahl. 2014. "Characterization of an Alluvial Silt and Clay Deposit for Monotonic, Cyclic, and Post-Cyclic Behavior." *Canadian Geotechnical Journal* 51, no. 4 (April): 432–440. https://doi.org/10.1139/cgj-2013-0057

Darendeli, M. B. "Development of a New Family of Normalized Modulus Reduction and Material Damping Curves." PhD diss., University of Texas at Austin, 2001.

Derakhshandi, M., E. M. Rathje, K. Hazirbaba, and S. M. Mirhosseini. 2008. "The Effect of Plastic Fines on the Pore Pressure Generation Characteristics of Saturated Sands." *Soil Dynamics and Earthquakes Engineering* 28, no. 5 (May): 376–386. https://doi.org/10.1016/j.soildyn.2007.07.002

Dobry, R., R. S. Ladd, F. Y. Yokel, R. M. Chung, and D. Powell. 1982. *Prediction of Pore Water Pressure Buildup and Liquefaction of Sands during Earthquakes by the Cyclic Strain Method, NBS Building Science Series 138*. Gaithersburg, MD: National Bureau of Standards.

Dobry, R., W. Pierce, R. Dyvik, G. E. Thomas, and R. Ladd. 1985. *Pore Pressure Model for Cyclic Straining of Sand*. Troy, NY: Rensselaer Polytechnic Institute.

Donaldson, A. M. "Characterization of the Small-Strain Stiffness of Soils at an In-Situ Liquefaction Test Site." Master's thesis, Oregon State University, 2019.

Fontana, D., S. Amoroso, L. Minarelli, and M. Stefani. 2019. "Sand Liquefaction Induced by a Blast Test: New Insights on Source Layer and Grain-Size Segregation Mechanisms (Late Quaternary, Emilia, Italy)." *Journal of Sedimentary Research* 89, no. 1 (January): 13–27. https://doi.org/10.2110/jsr.2019.1

Geodaq. 2014. *i6 Series In-Place Inclinometer*. Sacramento, CA: Geodaq Inc.

Gianella, T. N. and A. W. Stuedlein. 2017. "Performance of Driven Displacement Pile-Improved Ground in Controlled Blasting Field Tests." *Journal of Geotechnical and Geoenvironmental Engineering* 143, no. 9 (September): 04017047. https://doi.org/10.1061/(ASCE)GT.1943-5606.0001731

Gohl, W. B., J. A. Howie, and C. E. Rea. 2001. "Use of Controlled Detonation of Explosives for Liquefaction Testing." In *Fourth International Conference on Recent Advances in Geotechnical Earthquake Engineering and Soil Dynamics*, 9.13. Rolla, MO: Scholar's Mine.

Gohl, W. B., M. G. Jefferies, J. A. Howie, and D. Diggle. 2000. "Explosive Compaction: Design, Implementation and Effectiveness." *Geotechnique* 50, no. 6 (December): 657–665. https://doi.org/10.1680/geot.2000.50.6.657

Gohl, W. B., T. O. D. D. Martin, and R. J. Elliott. 2009. "Explosive Compaction of Granular Soils and In Situ Liquefaction Testing Using Sequential Detonation of Explosives." In *International Symposium on Ground Improvement Technologies and Case Histories*, 199–208. Singapore: Research Publishing.

Gohl, W. B., S. Tsujino, G. Wu, N. Yoshida, J. A. Howie, and J. Everard. 1998. "Field Applications of Explosive Compaction in Silty Soils and Numerical Analysis." In *Geotechnical Earthquake Engineering and Soil Dynamics III*, 654–665. Reston, VA: American Society of Civil Engineers.

Grigoli, F., S. Cesca, T. Dahm, and L. Krieger. 2012. "A Complex Linear Least-Squares Method to Derive Relative and Absolute Orientations of Seismic Sensors." *Geophysical Journal International* 188, no. 3 (January): 1243–1254. https://doi.org/10.1111/j.1365-246X.2011.05316.x

Heelan, P. A. 1953. "Radiation from a Cylindrical Source of Finite Length." *Geophysics* 18, no. 3 (July): 685–696. https://doi.org/10.1190/1.1437923

Henke, R. and W. Henke. 2002. "In Situ Nonlinear Inelastic Shearing Deformation Characteristics of Soil Deposits Inferred Using the Torsional Cylindrical Impulse Shear Test." *Bulletin of the Seismological Society of America* 92, no. 5 (June): 1970–1983. https://doi.org/10.1785/0120000273

Hsu, C. C. and M. Vucetic. 2006. "Threshold Shear Strain for Cyclic Pore-Water Pressure in Cohesive Soils." *Journal of Geotechnical and Geoenvironmental Engineering* 132, no. 10 (October): 1325–1335. https://doi.org/10.1061/(ASCE)1090-0241(2006)132:10(1325)

Idriss, I. M. and R. W. Boulanger. 2008. *Soil Liquefaction during Earthquakes: EERI Monograph No. 12*. Oakland, CA: Earthquake Engineering Research Institute.

InvenSense. 2013. *MPU-6000 and MPU-6050 Product Specification Revision 3.4, PS-MPU- 6000A–00*. San Jose, CA: InvenSense.

Jurkevics, A. 1988. "Polarization Analysis of Three-Component Array Data." *Bulletin of the Seismic Society of America* 78, no. 5 (October): 1725–1743.

Kramer, S. L. 1996. *Geotechnical Earthquake Engineering*. Upper Saddle River, NJ: Prentice Hall.

Kramer, S. L., S. S. Sideras, and M. W. Greenfield. 2016. "The Timing of Liquefaction and Its Utility in Liquefaction Hazard Evaluation." *Soil Dynamics and Earthquake Engineering* 91 (December): 133–146. https://doi.org/10.1016/j.soildyn.2016.07.025

Kurtulus, A. and K. H. Stokoe II. 2008. "In Situ Measurement of Nonlinear Shear Modulus of Silty Soil." *Journal of Geotechnical and Geoenvironmental Engineering* 134, no. 10 (October): 1531–1540. https://doi.org/10.1061/(ASCE)1090-0241(2008)134:10(1531)

Lee, K. L. and A. Albaisa. 1974. "Earthquake Induced Settlements in Saturated Sands." *Journal of the Geotechnical Engineering Division* 100, no. 4: 387–406.

Machan, G. and V. G. Bennett. 2008. *Use of Inclinometers for Geotechnical Instrumentation on Transportation Projects*. Washington, DC: Transportation Research Board.

Matasović, N. and M. Vucetic. 1992. "A Pore Pressure Model for Cyclic Straining of Clay." *Soils and Foundations* 32, no. 3 (September): 156–173. https://doi.org/10.3208/sandf1972.32.3_156

Matasović, N. and M. Vucetic. 1995. "Generalized Cyclic-Degradation-Pore-Pressure Generation Model for Clays." *Journal of Geotechnical Engineering* 121, no. 1 (January): 33–42. https://doi.org/10.1061/(ASCE)0733-9410(1995)121:1(33)

Mayne, P. W. 2007. *Cone Penetration Testing, NCHRP 368*. Washington, DC: Transportation Research Board.

Menq, F. Y. "Dynamic Properties of Sandy and Gravelly Soils." PhD diss., University of Texas at Austin, 2003.

Mikkelsen, P. E. and G. E. Green. 2003. "Piezometers in Fully Grouted Boreholes." In *Sixth International Symposium Field Measurements in Geomechanics*, 545–553. London: CRC Press.

Mortezaie, A. and M. Vucetic. 2016. "Threshold Shear Strains for Cyclic Degradation and Cyclic Pore Water Pressure Generation in Two Clays." *Journal of Geotechnical and Geoenvironmental Engineering* 142, no. 5 (May): 04016007. https://doi.org/10.1061/(ASCE)GT.1943-5606.0001461

Ohara, S. and H. Matsuda. 1988. "Study on Settlement of Saturated Clay Layer Induced by Cyclic Shear." *Soils and Foundations* 28, no. 3 (September): 103–113. https://doi.org/10.3208/sandf1972.28.3_103

Rathje, E. M., W. J. Chang, and K. H. Stokoe II. 2005. "Development of an In Situ Dynamic Liquefaction Test." *Geotechnical Testing Journal* 28, no. 1 (January): 50–60. https://doi.org/10.1520/GTJ12289

Riemer, M. F. and D. Cobos-Roa. 2007. "In Situ Measurement of Dynamic Properties Using the Downhole Freestanding Shear Device." In *Fourth International Conference on Earthquake Geotechnical Engineering*, edited by K. Pitilakis, 110. Dordrecht, the Netherlands: Springer Netherlands.

Roberts, J. N., K. H. Stokoe II, B. Cox, and F. Menq. 2017. "Field and Laboratory Investigations into the Behaviors of Silty Sands that Leads to Liquefaction Triggering." In *16th World Conference on Earthquake, 16WCEE 2017 Santiago Chile, January 9th to 13th 2017*. Chilean Association of Seismology and Earthquake Engineering.

Roberts, J. N., K. H. Stokoe II, S. Hwang, B. R. Cox, Y. Wang, F. M. Menq, and S. van Ballegooy. 2016. "Field Measurements of the Variability in Shear Strain and Pore Pressure Generation in Christchurch Soils." In *Fifth International Conference on Geotechnical and Geophysical Site Characterisation*, 627–632. St. Ives, Australia: Australian Geomechanics Society.

Robertson, P. K. and C. E. Wride. 1998. "Evaluating Cyclic Liquefaction Potential Using the Cone Penetration Test." *Canadian Geotechnical Journal* 35, no. 3 (June): 442–459. https://doi.org/10.1139/t98-017

Rollins, K. M., T. M. Gerber, J. D. Lane, and S. A. Ashford. 2005. "Lateral Resistance of a Full-Scale Pile Group in Liquefied Sand." *Journal of Geotechnical Geoenvironmental Engineering* 131, no. 1 (January): 115–125. https://doi.org/10.1061/(ASCE)1090-0241(2005)131:1(115)

Rollins, K. M., J. D. Lane, E. Dibb, S. A. Ashford, and A. G. Mullins. 2005. "Pore Pressure Measurement in Blast-Induced Liquefaction Experiments." *Transportation Research Record* 1936, no. 1 (January): 210–220. https://doi.org/10.1177/0361198105193600124

Sahadewa, A., D. Zekkos, R. D. Woods, and K. H. Stokoe II. 2015. "Field Testing Method for Evaluating the Small-Strain Shear Modulus and Shear Modulus Nonlinearity of Solid Waste." *Geotechnical Testing Journal* 38, no. 4 (July): 427–441. https://doi.org/10.1520/GTJ20140016

Sánchez-Salinero, I., J. M. Roesset, and K. H. Stokoe II. 1986. *Analytical Studies of Wave Propagation and Attenuation*. Washington, DC: Air Force Office of Scientific Research.

Stokoe, K. H., II, S. K. Hwang, N. K. J. Lee, and R. D. Andrus. 1995. "Effect of Various Parameters on the Stiffness and Damping of Soils at Small to Medium Strains." In *First International Symposium on Pre-failure Deformation of Geomaterials*, 785–816. Rotterdam, the Netherlands: A. A. Balkema.

Stokoe, K. H., II, J. N. Roberts, S. Hwang, B. Cox, F. Menq, and S. van Ballegooy. 2014. "Effectiveness of Inhibiting Liquefaction Triggering by Shallow Ground Improvement Methods: Initial Field Shaking Trials with T-Rex at One Site in Christchurch, New Zealand." In *New Zealand – Japan Workshop on Soil Liquefaction during Recent Large-Scale Earthquakes*, 193–202. Boca Raton, FL: CRC Press.

Tréhu, A. M. 1984. "Lateral Velocity Variations in the Orozco Transform Fault Inferred from Observed Incident Angles and Azimuths of P-Waves." *Geophysical Journal International* 77, no. 3 (June): 711–728. https://doi.org/10.1111/j.1365-246X.1984.tb02217.x

van Ballegooy, S., J. N. Roberts, K. H. Stokoe, B. R. Cox, F. J. Wentz, and S. Hwang. n.d. "Large-Scale Testing of Shallow Ground Improvements Using Controlled Staged-Loading with T-Rex." Paper presented at the Sixth International Conference on Earthquake Geotechnical Engineering, Christchurch, New Zealand, November 1–4, 2015.

Vucetic, M. 1994. "Cyclic Threshold Shear Strains in Soil." *Journal of Geotechnical Engineering* 120, no. 12 (December): 2208–2228. https://doi.org/10.1061/(ASCE)0733-9410(1994)120:12(2208)

Vucetic, M. and R. Dobry. 1986. *Pore Pressure Buildup and Liquefaction of Level Sandy Sites during Earthquakes, Report Number 86–3*. Troy, NY: Rensselaer Polytechnic Institute.

Vucetic, M. and R. Dobry. 1988. "Degradation of Marine Clays under Cyclic Loading." *Journal of Geotechnical Engineering* 114, no. 2 (February): 133–149.

Vucetic, M. and R. Dobry. 1991. "Effect of Soil Plasticity on Cyclic Response." *Journal of Geotechnical Engineering* 117, no. 1 (January): 89–107. https://doi.org/10.1061/(ASCE)0733-9410(1991)117:1(89)

Wentz, F., S. van Ballegooy, K. Rollins, S. Ashford, and M. Olsen. 2015. "Large Scale Testing of Shallow Ground Improvements Using Blast-Induced Liquefaction." Paper presented at the Sixth International Conference on Earthquake Geotechnical Engineering, Christchurch, New Zealand, November 1–4, 2015.

Wijewickreme, D., A. Soysa, and P. Verma. 2019. "Response of Natural Fine-Grained Soils for Seismic Design Practice: A Collection of Research Findings from British Columbia, Canada." *Soil Dynamics and Earthquake Engineering* 124 (September): 280–296. https://doi.org/10.1016/j.soildyn.2018.04.053

Wilson, S. D. and P. E. Mikkelsen. 1977. *Foundation Instrumentation—Inclinometers, FHWA TS-77-219*. Washington, DC: U.S. Department of Transportation.

Zeng, X. and G. McMechan. 2006. "Two Methods for Determining Geophone Orientations from VSP Data." *Geophysics* 71, no. 4 (July): V87–V97. https://doi.org/10.1190/1.2208935

Zha, Y., S. C. Webb, and W. Menke. 2013. "Determining the Orientations of Ocean Bottom Seismometers Using Ambient Noise Correlation." *Geophysical Research Letters* 40, no. 14 (August): 3585–3590. https://doi.org/10.1002/grl.50698

Zhang, B., K. H. Stokoe II, and F. M. Menq. 2019. "Field Measurement of Linear and Nonlinear Shear Moduli During Large-Strain Shaking." In *Seventh International Conference on Earthquake Geotechnical Engineering*. Rotterdam, the Netherlands: A. A. Balkema.